FRONTIERS OF PHYSICS

TOPICAL REVIEW
Volume 18 / Issue 5 / 53602 / 2023

Detecting nanoparticles by "listening"

Haonan Chang[1,2], Jun Zhang[1,2,†]

1 State Key Laboratory of Superlattices and Microstructures, Institute of Semiconductors, Chinese Academy of Sciences, Beijing 100083, China
2 Center of Materials Science and Optoelectronics Engineering, University of Chinese Academy of Sciences, Beijing 100049, China
Corresponding author. E-mail: †zhangjwill@semi.ac.cn
Received February 6, 2023; accepted March 24, 2023

ABSTRACT

In the macroscopic world, we can obtain some important information through the vibration of objects, that is, listening to the sound. Likewise, we can also get some information of the nanoparticles that we want to know by the means of "listening" in the microscopic world. In this review, we will introduce two sensing methods (cavity optomechanical sensing and surface-enhanced Raman scattering sensing) which can be used to detect the nanoparticles. The cavity optomechanical systems are mainly used to detect sub-gigahertz nano particle or cavity vibrations, while surface-enhanced Raman scattering is a well-known technique to detect molecular vibrations whose frequency generally exceeds terahertz. Therefore, the vibrational information of nanoparticles from low-frequency to high-frequency could be obtained by these two methods. The size of the viruses is at the nanoscale and we can regard it as a kind of nanoparticles. Rapid and ultrasensitive detection of the viruses is the key strategies to break the spread of the viruses in the community. Cavity optomechanical sensing enables rapid, ultrasensitive detection of nanoparticles through the interaction of light and mechanical oscillators and surface-enhanced Raman scattering is an attractive qualitatively analytical technique for chemical sensing and biomedical applications, which has been used to detect the SARS-CoV-2 infected. Hence, investigation in these two fields is of vital importance in preventing the spread of the virus from affecting human's life and health.

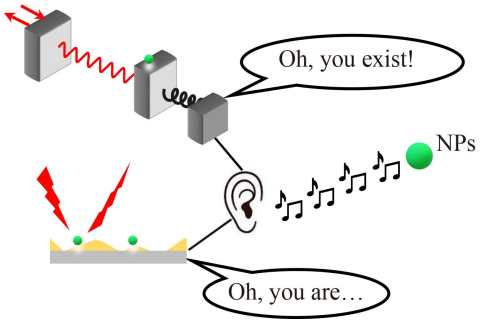

Keywords ultrasensitive sensing, cavity optomechanics, surface-enhanced Raman scattering

Contents

Higher Education Press

https://doi.org/10.1007/s11467-023-1287-1

1 Introduction

The detection and imaging of nanoparticles in microscopic systems has opened the door to understanding the microscopic world. In the past few decades, the detection and imaging of microscopic particles by optical methods [1–4], mechanical methods [5–12], and magnetic methods [13, 14] have been widely studied. Among them, the detection of nanoparticles by optical methods is the most widely used detection method [15]. The principle of optical sensing is that the presence of nanoparticles induces changes in optical microcavity transmission or reflection spectra, such as mode splitting [1], frequency shifting and mode broadening [2]. The interaction of light and matter can be enhanced by high-Q optical microcavity [15], plasmon [4], exceptional point enhancement [3] and so on, which would improve the measurement accuracy and sensitivity.

The vibration of nanoparticles contains rich information, and the detection of nanoparticles can be realized through the vibration of nanoparticles, that is, the detection of nanoparticles by mechanical methods, including electromechanical methods and optomechanical methods [5, 8, 10, 11]. Microelectromechanical systems (MEMS) can convert mechanical, chemical signals or other sensing singles into electrical signals [16, 17], which could make ultrasensitive biosensors because field-effect transistors combine efficient transducers with signal amplifiers in which a small parameter alteration induces a pronounced change of channel current [18, 19]. For example, Liqian Wang and his colleagues implemented an electromechanical biosensor for the detection of SARS-CoV-2 at ultralow concentrations via liquid-gated graphene field-effect transistor [11]. However, not all the MEMS could detect the vibration of nanoparticles, but nanoparticles affect the effective mass of MEMS or dielectric environment which changes its frequency, line width, and so on. Besides, the vibration frequency of the nanoparticles needs to be similar to the vibration frequency of the MEMS in order to achieve the measurement of the vibration modes. Raman spectroscopy is the most appropriate method for measuring high-frequency vibrational eigenmodes [20–22].

In this review, we focus on cavity optomechanical sensing and SERS for nanoparticle detection. The existence [5], mass [8, 23–30], and vibration modes [10] of nanoparticles have been detected at ultrahigh precision via cavity optomechanical systems until now. However, qualitative detection for nanoparticles, such as viruses, in cavity optomechanical systems is still a problem. SERS is an ultrasensitive qualitative detection method [9]. SERS provides high sensitivity originated from the amplified local electro-magnetic field in plasmonic nanostructures [1, 6, 7, 12, 31], which cannot be provided by spontaneous Raman scattering process. In the following, we will introduce the principles, platforms and the latest progress of cavity optomechanical sensing and SERS and the research perspectives in the future.

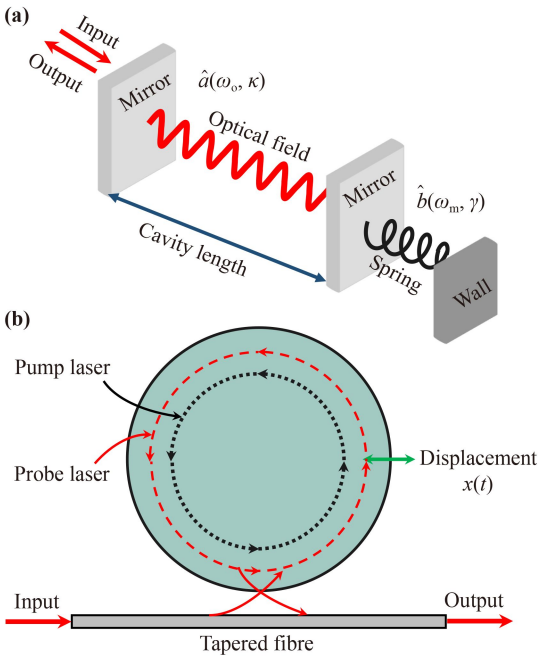

Fig. 1 **(a)** Schematic diagram of the cavity optomechanical coupling mechanism based on radiation pressure. **(b)** Whispering-gallery-mode microcavity-based optomechanics.

2 "Listening" to nanoparticles by ultrasensitive cavity optomechanical sensing

2.1 Basic principle of the cavity optomechanics

Cavity optomechanics enhances the interaction between electromagnetic radiation and mechanical motion via microcavities [32, 33]. The optomechanical coupling mechanism based on radiation pressure is shown in Fig. 1(a). The optical Fabry–Pérot cavity contains a stationary mirror and a movable mirror mounted on a spring. The intracavity photons with momentum $\hbar\boldsymbol{k}$, where $\hbar$ is the reduced Planck's constant, reflected off the movable mirror transfers a momentum $2\hbar\boldsymbol{k}$ onto the mirror due

to the law of conservation of momentum.

The displacement of the moveable mirror results in a change in the cavity length L, which changes the optical resonance frequency. The detuning between pump frequency and cavity resonance frequency determines the light amplitude inside the cavity, which subsequently leads to change of the cavity length. Hence, it creates a loop: the number of photons inside the cavity causes the radiation pressure force and the displacement of the mirror, and the radiation pressure effectively depends on the mirror position. As a result, the output photocurrent $i(t)$ experiences a periodic modulation, with a frequency corresponding to the mechanical frequency, and an amplitude proportional to the displacement and linearized optomechanical coupling strength. The whispering-gallery-mode (WGM) microcavity is a typical high-Q optomechanical system, which has been used widely in high-precision sensing [5, 8, 10, 34]. The above optomechanical coupling mechanism is applicable to WGM microcavities by replacing the cavity length L with the microcavity's radius r as shown in Fig. 1(b). The circulating photons exert radial radiation pressure on microcavities and induce structural deformation [35].

To precisely model the cavity optomechanical coupling process, a quantum theory is introduced to depict the cavity optomechanical coupling. The phonons and photons are both bosons, which can be pictured as quantized bosonic fields. Here, a typical cavity optomechanical system composed of a single optical cavity mode and a mechanical resonator is shown in Fig. 1(a). The total Hamiltonian $\widehat{H}_{\rm tot}$ of the system can be written as

$$\widehat{H}_{\rm tot} = \widehat{H}_{\rm drive} + \widehat{H}_0 + \widehat{H}_{\rm int}, \tag{1}$$

where $\widehat{H}_{\rm drive}$ is the optical driving of the system, $\widehat{H}_0$ is the uncoupled optical ($\omega_{\rm o}$) and mechanical ($\omega_{\rm m}$) modes, and $\widehat{H}_{\rm int}$ is the interaction part of the system's Hamiltonian.

When a continuous-wave laser used to pump the system, and the drive part of the system's Hamiltonian is written as

$$\widehat{H}_{\rm drive} = \hbar(\Omega^* {\rm e}^{{\rm i}\omega_L t}\widehat{a} + {\rm h.c.}), \tag{2}$$

where ω_L is the frequency of the pump laser, $\widehat{a}$ ($\widehat{a}^\dagger$) is the bosonic annihilation (creation) operator of the cavity optical mode, and Ω denotes the driving strength. The driving strength Ω can be expressed as

$$\Omega = \sqrt{\kappa_{\rm ex} P/(\hbar\omega_{\rm L})}{\rm e}^{{\rm i}\phi}, \tag{3}$$

where $\kappa_{\rm ex}$ is the decay rate of input-cavity coupling, P is the input laser power and ϕ is the initial phase of the pump laser.

The uncoupling part of the system's Hamiltonian can be described as

$$\widehat{H}_0 = \hbar\omega_{\rm o}\widehat{a}^\dagger\widehat{a} + \hbar\omega_{\rm m}\widehat{b}^\dagger\widehat{b}, \tag{4}$$

where $\widehat{b}$ ($\widehat{b}^\dagger$) is the bosonic annihilation (creation) operator of the mechanical mode. The displacement operator of the mechanical mode is given by

$$\widehat{x} = x_{\rm zpf}(\widehat{b}^\dagger + \widehat{b}), \tag{5}$$

where $x_{\rm zpf} = \sqrt{\frac{\hbar}{2m_{\rm eff}\omega_{\rm m}}}$ is the zero-point fluctuation, and $m_{\rm eff}$ is the effective mass of the mechanical mode.

The interaction part of the system's Hamiltonian can be described as

$$\widehat{H}_{\rm int} = \hbar g_0 \widehat{a}^\dagger\widehat{a}\left(\widehat{b}^+ + \widehat{b}\right), \tag{6}$$

where $g_0 = x_{\rm zpf}\cdot(\partial\omega_{\rm o}/\partial x)$ is the vacuum optomechanical coupling strength, expressed as a frequency, which quantifies the interaction between a single phonon and a single photon. The radiation pressure can be obtained as the derivation of $\widehat{H}_{\rm int}$ with respect to displacement:

$$F_{\rm rp} = -\frac{\partial\widehat{H}_{\rm int}}{\partial x} = \frac{\hbar g_0}{x_{\rm zpf}}\widehat{a}^\dagger\widehat{a}. \tag{7}$$

Typically, the driving part of the optomechanical system's Hamiltonian is described by Δ, where $\omega_{\rm L} = \omega_{\rm o} + \Delta$; conventionally, $\Delta < 0$ ($\Delta > 0$) is termed red (blue) detuning. In the frame rotating with the driving field, the system's Hamiltonian transforms to

$$\begin{aligned}\widehat{H}' =& \hbar\omega_{\rm m}\widehat{b}^\dagger\widehat{b} - \hbar\Delta\widehat{a}^\dagger\widehat{a} - \hbar g_0\widehat{a}^\dagger\widehat{a}\left(\widehat{b}^+ + \widehat{b}\right)\\ &+ \hbar(\Omega^*\widehat{a} + {\rm h.c.}),\end{aligned} \tag{8}$$

which can be obtained by applying the unitary transformation $\widehat{U} = {\rm e}^{{\rm i}\omega_L\widehat{a}^\dagger\widehat{a}t}$ to make the driving terms time independent.

The analytical treatment of the radiation-pressure dynamical backaction phenomena in the cavity optomechanical system can be described by quantum Langevin equations. The quantum Langevin equations are given by

$$\begin{aligned}\dot{\widehat{a}} =& -\frac{\kappa}{2}\widehat{a} + {\rm i}\left(\Delta + \frac{\partial\omega_o}{\partial x}\widehat{x}\right)\widehat{a} - {\rm i}\Omega\\ &- \sqrt{\kappa_{\rm ex}}\widehat{a}_{\rm in,ex} - \sqrt{\kappa_0}\widehat{a}_{\rm in,0},\end{aligned} \tag{9}$$

$$\dot{\widehat{b}} = \left(-{\rm i}\omega_{\rm m} - \frac{\gamma}{2}\right)\widehat{b} - {\rm i}g_0\widehat{a}^\dagger\widehat{a} - \sqrt{\gamma}\widehat{b}_{\rm in}, \tag{10}$$

where κ_0 is the intrinsic cavity decay rate, $\kappa = \kappa_{\rm ex} + \kappa_0$, which is the total optical decay rate, and γ is the damping rate of the mechanical mode. The quality factor of optical (mechanical) mode can be defined as $\kappa/\omega_{\rm o}$ ($\gamma/\omega_{\rm m}$). $\widehat{a}_{\rm in,ex}$, $\widehat{a}_{\rm in,0}$, and $\widehat{b}_{\rm in}$ are the noise operators of the intrinsic optical decay, external input-cavity coupling decay, and mechanical damping, respectively.

2.2 Key parameters of the cavity optomechanical sensing

The noise is an important factor to be considered in the optomechanical sensing, which could quantify the sensitivity of the optomechanical sensors, i.e., the minimum detectable signal in the optomechanical sensing. The noise in the optomechanical systems mainly includes thermal noise, shot noise and optomechanical backaction noise, where thermal noise is classical noise and shot noise and optomechanical noise is quantum noise.

Thermal noise is one of the fundamental limits to the precision of mechanical measurement. Before the discussion of the thermal noise, we first take a look at the mechanical measurement in optomechanical systems. The Newton equation of motion for a harmonic oscillator with effective mass m_{eff} is

$$\ddot{x} + \gamma_{\text{m}}\dot{x} + \omega_{\text{m}}^2 x = \frac{1}{m_{\text{eff}}}\left[F_{\text{d}}(t) + F_{\text{L}}(t)\right], \tag{11}$$

where $F_{\text{d}}(t)$ is driving force and $F_{\text{L}}(t)$ is Langevin force originating from thermal Brownian motion. In the experiment, we mainly concern about the mechanical displacement spectrum $x(\omega)$,

$$x(\omega) = \frac{1}{m_{\text{eff}}(\omega_{\text{m}}^2 - \omega^2) - \text{i}m_{\text{eff}}\gamma_{\text{m}}\omega}\left[F_{\text{d}}(\omega) + F_{\text{L}}(\omega)\right], \tag{12}$$

where the mechanical susceptibility χ_{xx} is defined as

$$\chi_{xx} = \frac{1}{m_{\text{eff}}(\omega_{\text{m}}^2 - \omega^2) - \text{i}m_{\text{eff}}\gamma_{\text{m}}\omega}. \tag{13}$$

The power spectrum density of the displacement $S_{xx}(\omega)$ is defined as the Fourier transformation of autocorrelation function of the displacement,

$$S_{xx}(\omega) = \int_{-\infty}^{+\infty}\langle x(0)\,x(t)\rangle \text{e}^{\text{i}\omega t}\text{d}t. \tag{14}$$

However, Eq. (14) is not applicable for the practical measurement. In the practical experiments, $S_{xx}(\omega)$ is measured in a limited duration τ,

$$S_{xx}(\omega) = \lim_{\tau\to\infty}\left\langle\left|\frac{1}{\sqrt{\tau}}\int_0^{\tau} x(t)\,\text{e}^{\text{i}\omega t}\text{d}t\right|^2\right\rangle. \tag{15}$$

The average displacement $\langle x^2\rangle$ can be obtained by the integration of the $S_{xx}(\omega)$,

$$\langle x^2\rangle = \int_{-\infty}^{+\infty} S_{xx}(\omega)\frac{\text{d}\omega}{2\pi}. \tag{16}$$

According to fluctuation dissipation theorem, we can get the $S_{xx}(\omega)$, thus we can get the average thermal motion

$$\langle x^2\rangle_{\text{th}} = \frac{k_{\text{B}}T}{m_{\text{eff}}\omega^2}, \tag{17}$$

where k_{B} is Boltzmann constant and T is temperature. The thermal noise can be suppressed by some measurement techniques, such as balanced homodyne detection.

The shot noise is because of the Heisenberg uncertainty relation that the number-phase for coherent states determines the limited precision of $\Delta\varphi\Delta N = 1/2$. When $\Delta = 0$, i.e., $\omega_{\text{L}} = \omega_{\text{o}}$, we can get the displacement power spectrum density induced by shot noise

$$S_{xx}^{\text{shot}}(\omega) = \frac{\kappa}{16\overline{n}_{\text{o}}g_0^2}\left[1 + 4\left(\frac{\omega}{\kappa}\right)^2\right], \tag{18}$$

where $\overline{n}_{\text{o}}$ is average photon number. When $\omega \ll \kappa$, $S_{xx}^{\text{shot}}(\omega)$ can be approximated as a constant and the shot noise is a white noise. Hence, we can reduce it by increasing the laser power. The optomechanical backaction noise originates from the radiation pressure force of photons acting on the mechanical resonator. The optomechanical backaction noise could be neglected in many optomechanical sensing experiments as a result from that the probe laser power is relatively low, to avoid thermal effect induced optical resonance shift.

The optomechanical measurement sensitivity of a physical quantity B (including displacement, force, etc.) at the frequency ω is determined by $\sqrt{S_{\text{BB}}(\omega)}$. Hence, the broad bandwidth and sensitivity are both important factors for optomechanical sensors. Thus, microtoroids are a good optomechanical sensing platform. Besides, the optomechanical coupling rate, decaying rate and quality factor are also important factors to be considered when designing the structure of the optomechanical sensors. We will introduce some structures of optomechanical sensors below.

2.3 Platforms for the cavity optomechanical sensing

In this review, the optomechanical sensing platforms are divided into passive optomechanical sensing platforms [27–29] and electrical modulated optomechanical sensing platforms (electro-optomechanical sensing platforms) [36–38] depending on whether there is an excitation source. The passive optical resonators placed on or close to the mechanical structures was the firstly developed field and it is used to perceive external stimuli. The vibration of the mechanical structures, usually suspended in the form of disks [39] or cantilever beams [40], will be optomechanically coupled into optical modes in the resonators, results in a wavelength shift of output signal [Fig. 2(a)] [41]. The second field, which has emerged in recent years, typically places internal stimuli through electrical modulation in the radio frequency (RF) range. Combining electrical resonance with external mechanical input will increase tunability and provide more degrees of freedom for sensitivity enhancement.

The passive optomechanical sensing platforms relies on larger displacement to induce change which is more prominent in the optomechanical systems for detection. The micro-cantilever is a typical mechanical input structure to interact with the environment, which has an

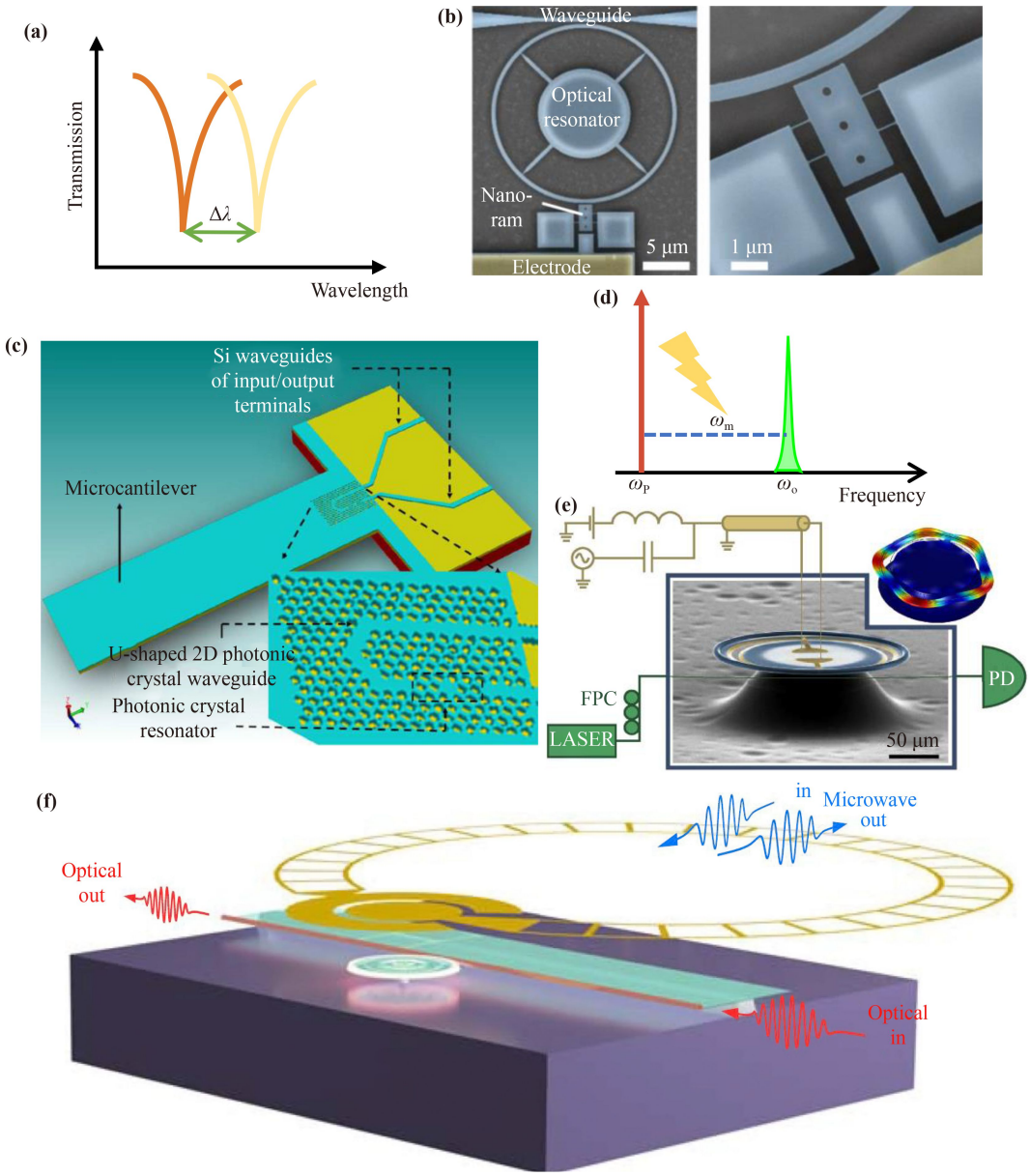

Fig. 2 Various cavity optomechanical coupling platforms. **(a)** The principle of the passive optomechanical coupling platforms. The passive optomechanical coupling elements consisting of micro-cantilevers **(b)** (Reproduced with permission from Ref. [29], Copyright © 2020 Nature) and microcavities **(c)** (Reproduced with permission from Ref. [41], Copyright © 2009 IEEE). **(d)** The principle of the electrical modulated optomechanical coupling platforms. **(e, f)** The electrical modulated optomechanical coupling platforms. (e) Reproduced with permission from Ref. [37], Copyright © 2017 The Optical Society of America. (f) Reproduced with permission from Ref. [36], Copyright © 2020 Nature.

advantage that using such a cantilever allows for larger mechanical deformation. Besides, the sensitivity will be improved by reducing the effective mass and dimensions. The typical optical readout configuration of the passive optomechanical sensing platforms is microdisk resonators [29] [Fig. 2(b)] and photonic crystal resonators [42–44] [Fig. 2(c)]. The cantilever-based optomechanical sensors can be divided into two main sections: photonic crystal cavities built on the cantilever leveraging the shape deformation of the optomechanical resonators, and cavity optomechanical coupling between the cantilever and microcavities. These types of optomechanical sensors are mainly found in chemical sensing [42] and atomic force microscopy applications [45, 46], where high precision sensitive measurements are needed. As shown in Fig. 2(b), the micro-cantilever coupling with microdisk performed mass spectrometry ranging from 2.8 to 7.7 MDa in less than 5 min and demonstrated excellent stability, which provides excellent toolboxes for optomechanical mass sensing of the viruses [29].

In the electro-optomechanical coupling platforms [36–38], piezoelectric-driven and electrostatic-driven are two mainstream approaches to probe and detune the optomechanical cavity modes and provide the bridge for energy exchange between phonons and photons as shown in Fig. 2(d) [37]. The acousto-optical interaction between stimulated acoustic phonons and light beams provides excellent possibilities for a new class of inertial sensing without movable structures, thus enhancing both the reliability and the tuning frequency. In 2017, Bekker *et al.* [38] demonstrated a radiation-pressure-driven cavity optomechanical system actuated and locked by an integrated electrical interface as shown in Fig. 2(e). The injection signal employed to suppress the drift in the optomechanical oscillation frequency could reduce the phase noise by over 55 dBc/Hz at 2 Hz offset. The electrical interface allows enhanced scalability for future applications associated with arrays of injection-locked precision sensors. In 2020, Han and his colleagues [37] reported that they aligned a 10-GHz piezoelectric-driven microwave resonator on the top of an optomechanical cavity [Fig. 2(f)], which enables resonant enhancement of optomechanical and electromechanical interactions simultaneously. The large piezo-mechanical cooperativity ($C_{\mathrm{em}} \sim 7$) and the enhanced optomechanical coupling boosted by a pulsed optical pump are achieved in this triply resonant piezo-optomechanical system based on the integrated interface between superconducting and nanophotonic circuits.

In recent years, optomechanical crystals with bound states in the continuum (BICs) are an emerging research field [47–51], which refer to a type of eigenstates with infinite lifetime yet spectrally overlapping with lossy states in the continuum [49]. The optomechanical crystals with BICs could reach ultrahigh optomechanical coupling rate and mechanical quality factor [49, 50], which results in high sensitivity to small changes in the phonon spectrum, thus the development of highly sensitive optomechanical sensors is one promising application of optomechanical crystals with BICs. Additionally, they can be fabricated using standard lithographic techniques [50], which makes them compatible with existing semiconductor processing technologies.

2.4 Optomechanical detection of the mass of the nanoparticles

According to Eq. (11), we can obtain the resonance frequency of mechanical resonator f_{m},

$$2\pi f_{\mathrm{m}} = \sqrt{\frac{k}{m_{\mathrm{eff}}}}, \tag{19}$$

where k is spring constant. When the nanoparticles or viruses are deposited on the surface of the mechanical oscillator, the effective mass of the harmonic oscillator changes. Qualitatively, we simply consider the deposited mass m_{d} as

$$m_{\mathrm{d}} = \delta m_{\mathrm{eff}} = -\frac{2m_{\mathrm{eff}}}{f_{\mathrm{m}}}\delta f_{\mathrm{m}}, \tag{20}$$

where δm_{eff} is the changes of the effective mass and δf_{m} is the change of the resonance frequency. Besides, the relationship between deposited mass and resonance frequency shift depends on the position of the deposited objects [8]. According to Eq. (20), we can get that the detection threshold (i.e., the smallest mass can be detected) of the measurement is related to the resonance frequency of the mechanical oscillator. Hence, design and fabrication of the high-frequency mechanical resonators [52–54] are of vital importance to improve the detection threshold and sensitivity of the optomechanical mass sensing.

There are many in-plane vibration modes in whispering-gallery optomechanical system [Fig. 3(a)], which favors their coupling to optical whispering gallery modes. In 2022, Sbarra and his colleagues [8] demonstrated multimode optomechanical sensing of single particles with a radius between 70 and 150 nm [Fig. 3(b)], which is approximately the size of the virus SARS-CoV-2 [55]. The optomechanical sensing principle is that an adsorption produces a mechanical frequency shift within point-mass approximation:

$$\delta f_{\mathrm{m}}/f_{\mathrm{m}} = -\left[m_{\mathrm{d}}/(2m_{\mathrm{eff}})\right] u(\boldsymbol{r}_0)^2, \tag{21}$$

where m_{eff} is the effective mass of the considered mechanical mode, m_{d} is the absorbed mass and $u(\boldsymbol{r}_0)^2$ is the normalized modal displacement at the analyte landing position $\boldsymbol{r}_0$. They performed multimode mechanical measurement of latex nanoparticles by simultaneously tracking both RBM1 and RBM2. The sensing accuracy is determined by mechanical quality factor Q_{m} and optomechanical coupling coefficient g_{om}. Hence, the signal from RBM2 was noisier, the phase jumped smaller and [Fig. 3(c)] the mass estimation was more inaccurate because of low Q_{m} and g_{om}, which suggests that high Q_{m} and g_{om} is necessary for optomechanical sensing. In their work, multiple mechanical and optical resonant signals can be obtained simultaneously, providing access to several pieces of physical information about the landing analyte in real time, which provides a novel way to detecting viruses in real time.

The above optomechanical mass sensing experiments are carried out in the linear optomechanical coupling regime [32], in which the frequency of a cavity mode is approximatively proportional to the displacement of a mechanical mode, i.e., $\omega_{\mathrm{o}}(x) \propto x$. In 2010, Sankey *et al.* [56] demonstrated that an optical cavity containing a flexible dielectric membrane enable us to realize the quadratic optomechanical coupling in experiment as shown in Fig. 4(b). In the pure quadratic optomechanical coupling regime, there is a linear relation between the position-dependent cavity resonance frequency and the

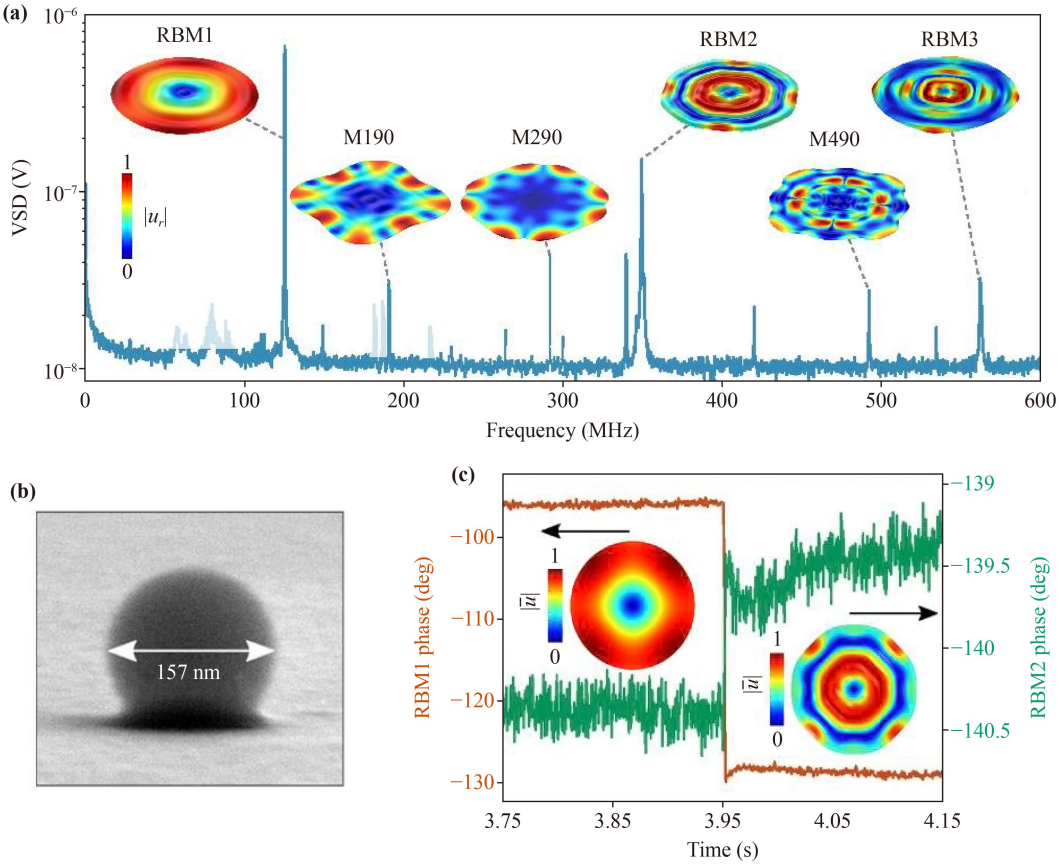

Fig. 3 Weigh a single nanoparticle by multimode optomechanical system. **(a)** Multimode optomechanical system. **(b)** SEM image of the 157 nm diameter nanoparticle. **(c)** Demodulated output signal phase at the resonance frequencies of the RBM1 (red) and RBM2 (green) during the landing of a cluster of three latex nanoparticles. Reproduced with permission from Ref. [8], Copyright © 2022 American Chemical Society.

square displacement of the membrane, i.e., $\omega(x) \propto x^2$. The quadratic optomechanical coupling has been used to induce unique optical phenomena including quantum phase transition, two-phonon optomechanical induced transparency and amplification, and the preparation of squeezed states and superposition states [24, 56–64]. In 2019, Liu and his colleagues [24] reported a novel optomechanical mass sensing scheme in theory that an added mass deposited on the dielectric membrane can be detected by the by monitoring the efficiency of variation of the second sideband generation.

As shown in Fig. 4(a), the model they studied is a membrane-in-the-middle optomechanical cavity and a degenerate parametric amplifier (DPA) [65, 66] is embedded into it. The membrane is designed with the prosperities that angular frequency ω_{m}, effective mass m_{m}, and finite reflectivity R. Besides, the nonlinear cavity optomechanical system is driven by a strong control field ω_{d} and probed by a weak probe pulse ω_{p}. In the optomechanical system, the effective frequency of the cavity is approximated to the second-order term of displacement:

$$\omega(x) = \omega_{\mathrm{c}} + \frac{1}{2}\frac{\partial^2\omega}{\partial x^2}x^2, \tag{22}$$

and the quadratic optomechanical coupling constant G is defined as [67, 68]

$$G = \frac{1}{2}\frac{\partial^2\omega}{\partial x^2}\bigg|_{x=0} = \frac{8\pi^2 c}{L\lambda_{\mathrm{d}}^2}\sqrt{\frac{R}{1-R}}, \tag{23}$$

where c is the speed of light in vacuum and λ_{d} is the wavelength of the control field. In their work, the parameters of quadratically coupled optomechanical system were obtained from Ref. [69]. The parameters are as follows: the angular frequency of the membrane $\omega_{\mathrm{m}} = 2\pi \times 0.1$ MHz, the mass of the membrane $m_{\mathrm{m}} = 100$ pg, the mechanical quality factor $Q_{\mathrm{m}} = \pi \times 10^4$, the reflectivity of the reflectivity $R = 0.45$, the cavity length $L = 67$ mm, and the total loss rate $\kappa = 0.2\omega_{\mathrm{m}}$. Besides, they assume the wavelength of control field $\lambda_{\mathrm{d}} = 532$ nm and the cavity mode detuning $\Delta = 2\omega_{\mathrm{m}}$ to build a two-phonon resonance case in the quadratic optomechanical coupling circumstance.

As shown in Figs. 4(c) and (d), when the added mass δm increases, the steady-state solution of GX_0 decreases

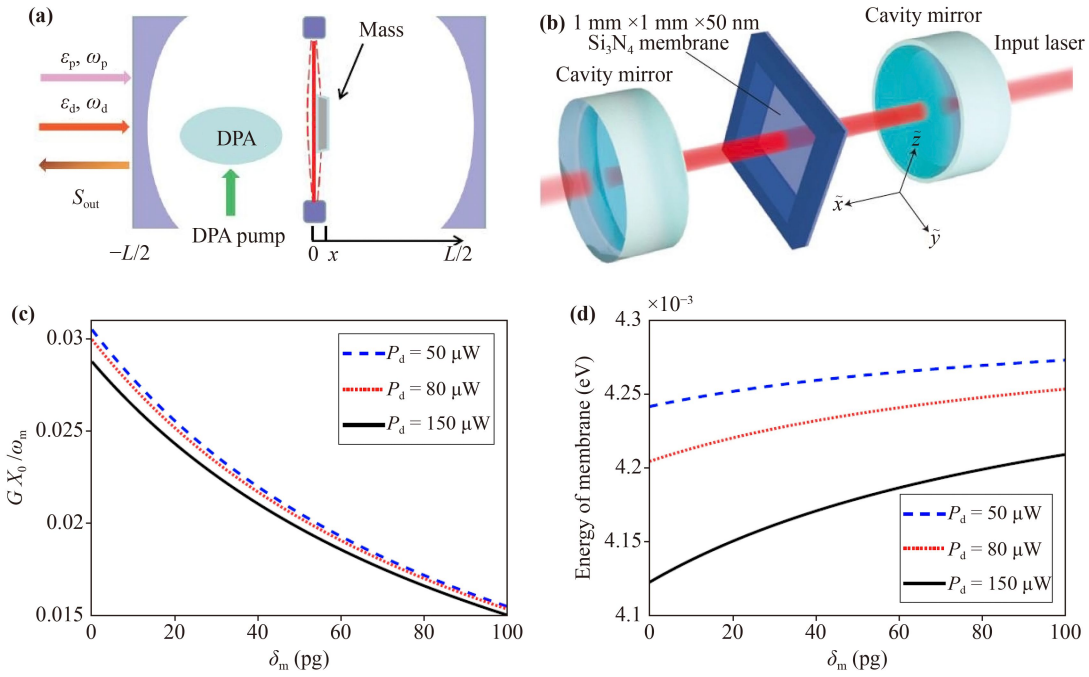

Fig. 4 Nonlinear cavity optomechanical systems for optomechanical mass sensing. **(a)** Schematic diagram of a quadratically coupled optomechanical system. A degenerate parametric amplifier (DPA) is embedded into a membrane-in-the-middle cavity driven by a strong control field ω_d and a weak probe pulse ω_p. Reproduced with permission from Ref. [24], Copyright © 2019 American Physical Society. **(b)** A quadratically coupled optomechanical platform in an experiment. Reproduced with permission from Ref. [55], Copyright © 2010 Nature. **(c)** The steady-state solution of GX_0 versus the added mass δm for different control field intensities P_d = 50 μW, 80 μW, and 150 μW. Reproduced with permission from Ref. [24], Copyright © 2019 American Physical Society. **(d)** The eigenenergy of a membrane versus the added mass δm for different control field intensities P_d = 50 μW, 80 μW, and 150 μW. Reproduced with permission from Ref. [24], Copyright © 2019 American Physical Society.

monotonically, while the eigenenergy of the membrane increases monotonically. Hence, they can deduce the added mass change in the quadratically coupled optomechanical system has a prominent influence on the steady-state solution of the system and the eigenenergy of the membrane. Besides, they derived explicitly analytical expressions for the efficiency of a second-order sideband and the sensitivity of a mass sensor beyond the conventional linearized approximation. In short, their work illustrates the potential to use the nonlinear dynamics of the quadratically coupled optomechanical system for designing an all-optical nonlinear mass sensor.

2.5 Optomechanical detection of the vibrational modes

The low-frequency vibration modes of proteins, viruses and bacteria in the terahertz and gigahertz domain [Fig. 5(b)] carry important information which may provide valuable information on the diagnosis of certain diseases [70]. However, the frequency of vibration modes of bacteria and viruses is too low to be detected by traditional optical tools, such as Raman spectrometry, and too high to be detected nanomechanical resonator. Gil-Santos *et al.* [10] fabricated ultrahigh frequency optomechanical disk resonators to detect the vibration modes of the bacterium [Fig. 5(a)] and the mechanical resonance frequency could reach or suppress the frequency of the vibration modes of the bacterium [10]. According to the ratios of sensor eigenfrequency (ω_S) to the fundamental eigenfrequency of the analyte (ω_A), the system's response can be classified into three regimes [Fig. 5(c)]: an inertial regime ($\Lambda \ll 1$), in which the resonance frequency redshifts due to the mass of the analyte; a coupling regime ($1 \leq \Lambda \leq \beta_2$), where β_2 is the ratio between the 2nd eigenfrequency of the analyte and its fundamental resonance frequency, in which two mechanical motions resonate with each other, or hybridize, inducing a doublet in the mechanical spectrum of the system from which the vibration characteristics of the analyte can be extracted; an insensitive regime ($\Lambda \gg \beta_2$), in which no information can be obtained. Gil-Santos *et al.* [10] implemented the experiment in the coupling regime and they detected the vibration modes of Staphylococcus epidermidis. Besides, they could monitor bacterium hydration by measuring its eigenfrequency and Q due to its porous structure. In a word, their work goes beyond detecting the presence or absence of analytes in the optomechanical system whereas previous optomechanical sensing experiments in the inertial regime only allows the detection of the presence or absence of the analytes. Their work

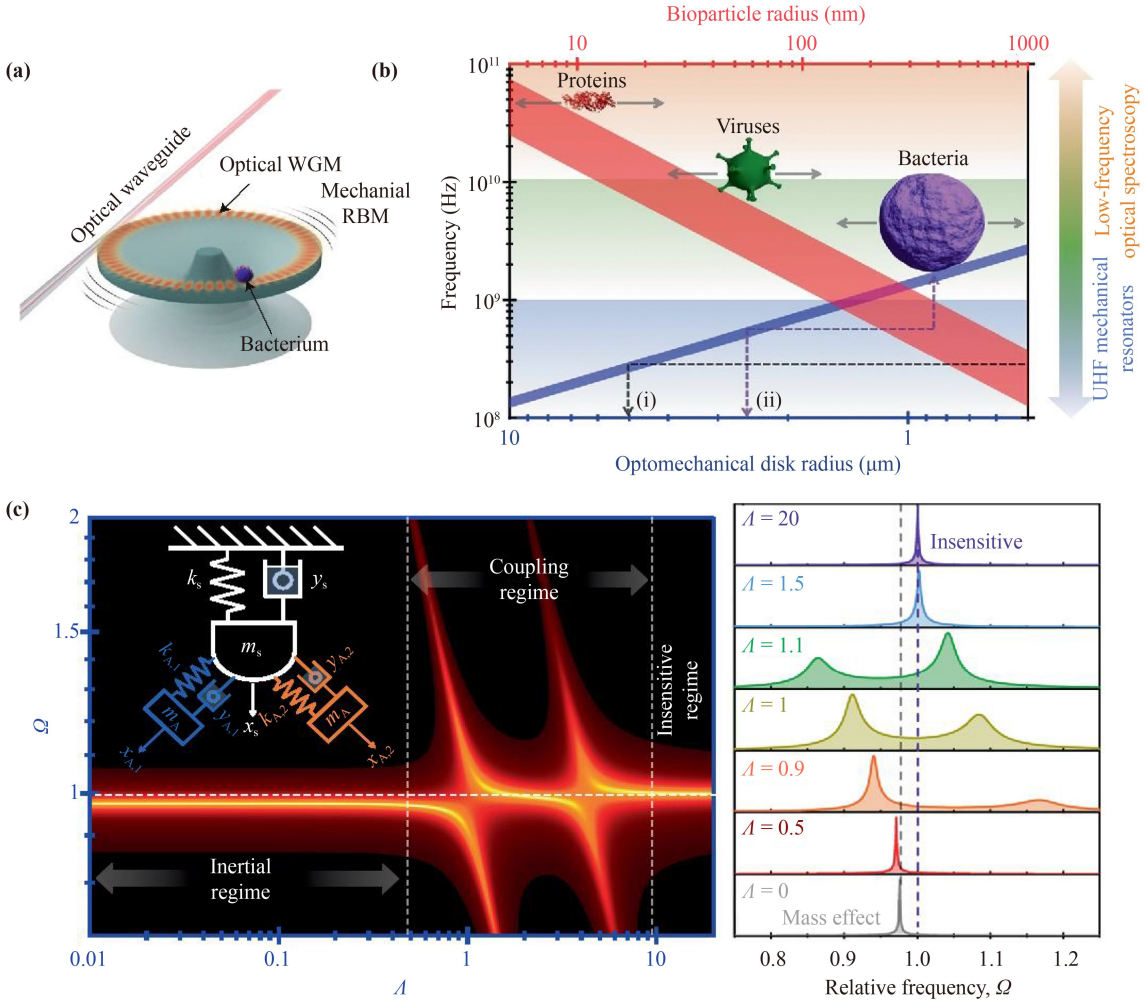

Fig. 5 Experimentally detect the vibration modes of a single bacterium via an optomechanical microcavity. **(a)** Experimental setup. **(b)** Frequency of the radial breathing mode of an optomechanical disk (blue region) and of the fundamental mode of quasi-spherical biological particles adsorbed on a rigid support (red region) as a function of the disk and bioparticle radii, respectively. **(c)** The left panel: Color-intensity map of the amplitude of the fluctuations of the sensor as a function of the dimensionless frequency and the ratio of the radial breathing mode eigenfrequency to the fundamental eigenfrequency of the particle (Λ). The right panel: Cross-sections of the regions in the left panel for $\Lambda = 0$, 0.5, 0.9, 1, 1.1, 1.5 and 20. The gray and purple vertical dashed lines represent the corresponding the values of Λ at the boundaries of the inertial region. Reproduced with permission from Ref. [69] and Ref. [10], Copyright © 2020 Nature.

paves a new way to detect bioparticles via cavity optomechanical system.

2.6 Cavity optomechanical spring sensing of single molecules

Single-molecule sensors are at the cutting edge of biochemical sensing field [71]. Yu *et al.* [5] reported the first single molecule sensing experiment based on the cavity optomechanical spring effect in 2016. They detected single bovine serum albumin proteins with a molecular weight of 66 kDa at a signal-to-noise ratio of 16.8. The schematic of cavity optomechanical spring sensing mechanism is shown in Fig. 6. In the high optical quality factor microsphere, the optical wave inside the microsphere produces a strong radiation pressure which efficiently drives the radial breathing mechanical motion of the microsphere. The mechanical resonance frequency f_{m} is dependent sensitively on the optical cavity detuning $\Delta = \lambda_1 - \lambda_0$, where λ_1 is the laser frequency and λ_0 is optical cavity resonance frequency. The particle or molecule binding on the microsphere induces a tiny perturbation to the cavity resonance wavelength $\delta\lambda$, which would be transferred to the mechanical resonance frequency shift δf_{m}, where $\delta f_{\mathrm{m}} = -\frac{\mathrm{d}f_{\mathrm{m}}}{\mathrm{d}\Delta}\delta\lambda$. Hence, an efficient transduction mechanism to amplify resonance wavelength sensing can be realized via optical spring effect. The sensing resolution can be determined by effective mechanical quality factor $Q_{\mathrm{m}} = f_{\mathrm{m}}/\delta f_{\mathrm{m}}$ of coherent optomechanical oscillation. The Q_{m} of the microsphere

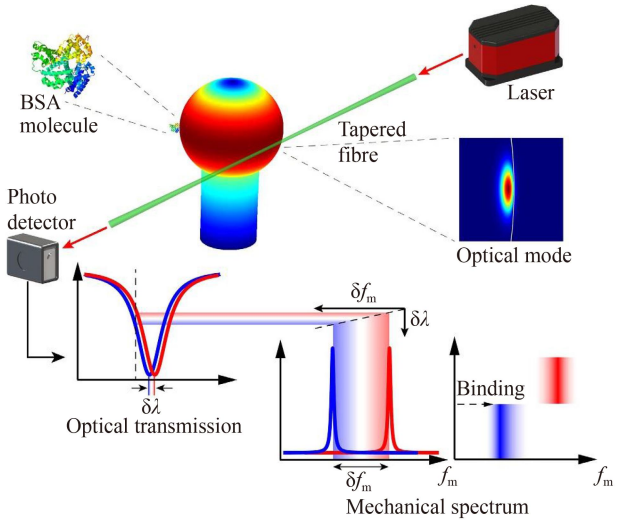

Fig. 6 Schematic diagram of the principle of detecting nanoparticles based on the whispering-gallery cavity optomechanical devices. Reproduced with permission from Ref. [5], Copyright © 2016 Nature.

device can reach a value above 10^6, resulting in a sensing resolution which is sufficient for single-molecule detection.

3 "Listening" to nanoparticles by SERS

3.1 Basic principle of SERS

Raman spectroscopy, which relies on the inelastic scattering of light to quantify the unique vibrational modes of molecules, has enabled accurate label free fingerprinting of individual viral components [72–79]. Figure 7 shows the schematic diagram of anti-Stokes and Stokes Raman scattering processes [80]. According to quantum mechanics, the Stokes (anti-Stokes) process consists of a transition to a virtual state, followed by a re-emission, leaving the molecule in the first vibrational excited state $\nu = 1$ (ground state $\nu = 0$), which corresponds to positive (negative) Raman shifts in the spectrum. The anti-Stokes process depends on the population of the excited level, while the Stokes one is independent of it, which lead to that Stokes process is stronger than anti-Stokes process in the Raman scattering generally. In the Raman scattering experiments, the efficiency of scattering processes is measured by a cross section σ, and the Stokes intensity I_S for an ensemble of N molecules with a pump laser power density I_L can be described by

$$I_S = N\sigma_S I_L(1+n), \tag{24}$$

where σ_S is the cross section of Stokes process and n is average phonon number. The anti-Stokes intensity is directly proportional to n, i.e.,

$$I_{aS} = N\sigma_{aS} I_L n, \tag{25}$$

where σ_{aS} is the anti-Stokes cross section.

However, the spontaneous Raman scattering could not provide the essential sensitivity to detect a low viral titer. SERS attracts increasing interest as an analytical technique for chemical sensing and biomedical applications due to several advantages, such as single-molecule sensitivity, unique spectral signatures of analytes, no interference from water, easy operation without complicated sample preparation [81–83]. The electromagnetic enhancement originating from the amplified local electromagnetic field in plasmonic nanostructures is typically the largest contributor to SERS (Fig. 8) [84], which would yield enhancements from 10^4 to 10^8 [85]. Besides, the chemical enhancement is also a contributor to SERS because of changes in the electronic structure of

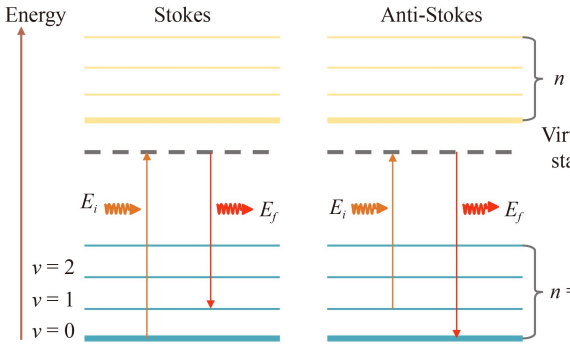

Fig. 7 Schematic diagram of Raman scattering process. The left panel is Stokes scattering process and the right panel is anti-Stokes scattering process. Reproduced with permission from Ref. [79], Copyright © 2008 Royal Society of Chemistry.

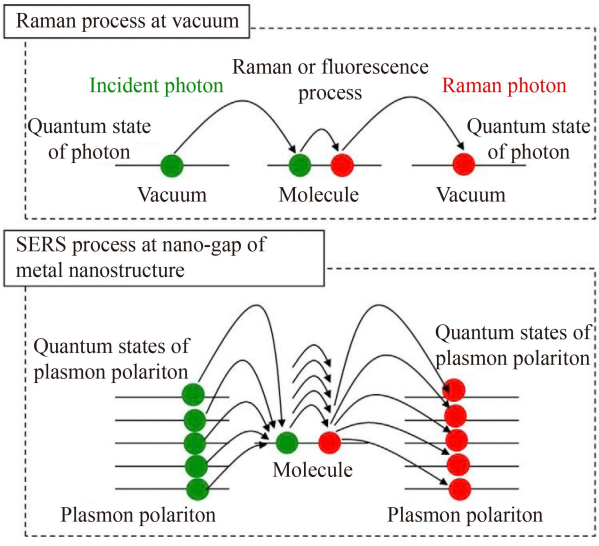

Fig. 8 Schematic diagram of Raman and SERS processes. The intensity of SES is enhanced by the existence of the plasmon polariton. Reproduced with permission from Ref. [83], Copyright © 2014 Elsevier.

molecules adsorbed on metal surfaces and it is usually interpreted by charge transfer mechanism [86, 87]. while the chemical enhancement process yields an enhancement factor only between 10 and 100 [85] and it is a great challenge to distinguish chemical enhancement from the electromagnetic mechanism [86–88]. The design and fabrication of plasmonic nanostructures is the key to the high-performance SERS sensors because the maximum field enhancement determines the sensitivity, reproducibility and applicability of the sensor.

The conventional explanation attributes the enhancement of SERS to the subwavelength confinement of the electromagnetic field near nanoantennas. However, it could not explain why the maximal enhancement was achieved when the laser was blue-detuned from the plasmon resonance by the vibrational frequency. Roelli and his colleagues [89, 90] revealed that the major enhancement of SERS originates from the amplified local electromagnetic field in plasmonic nanostructures, which can be understood as dynamical backaction amplification of molecular vibrations in the theoretical framework of cavity optomechanics (Fig. 9). The plasmon force F_{p} with an amplification factor proportional to the time-averaged intracavity plasmonic field and Raman polarizability $\mathrm{d}\alpha/\mathrm{d}x_\nu$, and thermal force F_{th} lead to the molecular displacement δx_ν. The molecular vibration changes the polarizability of the molecule, which in turn leads to a shift of the plasmon resonance frequency, closing the feedback looping, which could enhance the Raman scattering intensity under dynamical backaction amplification and sharpen the Raman excitation spectral linewidth.

In the cavity optomechanical system, the optomechanical coupling factor is of vital importance. We will introduce the vacuum optomechanical coupling factor of plasmonic resonance and molecule vibration. The change in resonance frequency ω_{P} of a cavity $\Delta\omega_{\mathrm{P}}$ when a dielectric is inserted in an air gap is described by

$$\Delta\omega_{\mathrm{P}} = -\frac{\omega_{\mathrm{P}}}{2}\frac{\int_V \boldsymbol{P}\cdot\boldsymbol{E}_{\mathrm{P}}\mathrm{d}V}{\int \varepsilon_0 \frac{\mathrm{d}(\omega\epsilon(\omega))}{\mathrm{d}\omega}|\boldsymbol{E}_{\mathrm{P}}|^2\mathrm{d}V}, \tag{26}$$

where $\boldsymbol{E}_{\mathrm{P}}$ is the plasmonic cavity field, $\boldsymbol{P}$ is the induced dipole per unit volume $\varepsilon(\omega)$ is dielectric constant, and ε_0 is dielectric constant in vacuum. The plasmonic cavity dimension is sufficiently small in comparison to the incoming wavelength, which contributes to that the quasistatic approximation remains valid and the magnetic energy can be neglected. Besides, we assume that a single molecule is located at the position of maximum electric field.

The molecular dipole moment $\boldsymbol{p}$ can be depicted as

$$\Delta\omega_{\mathrm{P}} \approx -\frac{\omega_{\mathrm{P}}}{2}\frac{\boldsymbol{p}\cdot\boldsymbol{E}_{\max}}{\frac{1}{2}\mu\int\varepsilon_0|\boldsymbol{E}_{\mathrm{P}}|^2\mathrm{d}V}, \tag{27}$$

where μ depends on the dielectric function of the metal and the plasmon resonance frequency. The relation

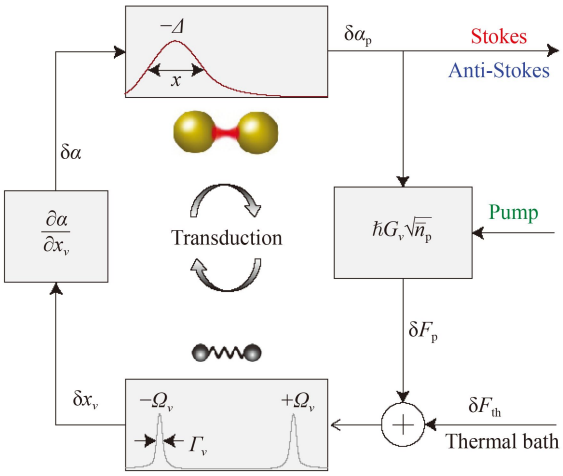

Fig. 9 Feedback diagram of dynamical backaction in the SERS process in the theoretical framework of cavity optomechanics. Reproduced with permission from Ref. [88], Copyright © 2015 Nature.

between dipole moment $\boldsymbol{p}$ and $\boldsymbol{E}_{\max}$ can be described by

$$\boldsymbol{p} = \alpha(x_\nu)\cdot\boldsymbol{E}_{\max} = \left[\alpha(0) + \frac{\partial\alpha}{\partial x_\nu}x_\nu\right]\cdot\boldsymbol{E}_{\max}, \tag{28}$$

where x_ν is the displacement of molecule vibration and α is the linear polarizability. The polarizability of the molecule includes the contributions from the internal electronic transition so that it is frequency dependent. Hence, we can obtain the sensitivity of the plasmonic frequency to the molecular vibrations:

$$G_{\mathrm{p}\nu} = \frac{\partial(\Delta\omega_{\mathrm{P}})}{\partial x_\nu} = -\frac{\omega_{\mathrm{P}}}{2}\frac{\frac{\partial\alpha}{\partial x_\nu}|\boldsymbol{E}_{\max}|^2}{\frac{1}{2}\mu\int\varepsilon_0|\boldsymbol{E}_{\mathrm{P}}|^2\mathrm{d}V} = -\frac{\omega_{\mathrm{P}}}{\varepsilon_0 V_{\mathrm{m}}}\frac{\partial\alpha}{\partial x_\nu}, \tag{29}$$

where V_{m} is the effective mode volume of the cavity mode,

$$V_{\mathrm{m}} = \frac{\mu\int|\boldsymbol{E}_{\mathrm{P}}|^2\mathrm{d}V}{|\boldsymbol{E}_{\max}|^2}. \tag{30}$$

When the plasmon resonance frequency gets closer to the bulk plasma resonance frequency, the energy stored in the metal grows and the mode volume increases. The single-photon optomechanical coupling rate can be obtained:

$$g_{\nu 0} = G_{p\nu}x_{zpm,\nu} = \frac{\omega_{\mathrm{p}}}{\varepsilon_0 V_{\mathrm{m}}}\frac{\partial\alpha}{\partial x_\nu} = \sqrt{\frac{\hbar}{2m_\nu\omega_\nu}}, \tag{31}$$

where m_ν is the effective mass of the molecule vibration and ω_ν is the frequency of the molecule vibration. In Philippe Roelli's paper, they calculated the vacuum optomechanical coupling rates $g_{\nu 0}/(2\pi)$, and obtained that $g_{\nu 0}/(2\pi)$ varies between 10^9 Hz to 10^{11} Hz, which is ultra-high compared with other cavity optomechanical systems.

3.2 SERS-active nanomaterials

According to the dimension of the nanomaterials, the SERS-active nanomaterials can be classified into four kinds: 0D, 1D, 2D, and 3D [91]. The typical noble metal-dependent 0D SERS-active materials are gold nanoparticles (Au NPs) [92] and silver nanoparticles (Ag NPs) [93] [Fig. 10(a)]. Au NPs have shown good chemical stability, excellent biocompatibility, unique electronic structure and outstanding localized surface plasmon resonance absorption properties. Ag NPs exhibit a superior Raman enhancement effect through the much stronger electromagnetic field between each particle under laser irradiation, owing to the prominent optical properties while the chemical stability of the Ag NPs is not as good as Au NPs. In 1997, Nie *et al.* [94] found that the intrinsic Raman enhancement factors increased on the order of 10^{14} to 10^{15} for single molecules absorbed on the Ag NPs. Besides, the shapes of metal NPs play a crucial role in enhancement of Raman signals. The typical shapes of the NPs include spheres, stars, triangles, clusters, and so on, which can be easily controlled by changing the reaction conditions, such as temperature, reaction volume, and the ratio of precursors [91]. To generate numerous so-called hot spots on the surface of NPs, many novel shapes of the NPs are designed, including flower-like nanostructures [95, 96], core–shell nanostructures [97–99], hollow-shell nanostructures [100, 101], etc.

The typical SERS-active 1D nanomaterials mainly include metal nanorods, nanorod bundles, and shuttle-like, wire-like or tube-like nanocrystals [Fig. 10(b)] [102]. However, the lengths of the above 1D nanomaterials reach the microscale, inducing that the hot spot only distribute at both endpoints, which limits the enhancement effect of the Raman signal. Building novel NPs on the extensive surfaces of the 1D nanomaterials to increase the number of hot spots is a good strategy. Kang and his colleagues [103] designed an Au particle-on-wire sensor, which could be applied for detection of multiple pathogen DNA by employing SERS technology. Besides, hollow nanowires, i.e., nanotubes could generate more hot spots due to their high specific surface areas [104].

The SERS-active 2D nanomaterials refer to monolayer materials, such as monolayer graphene/graphene oxide, monolayer molybdenum disulfide monolayer, monolayer black phosphorous [Fig. 10(c)] [105–107]. The 2D nanomaterial substrates can provide certain wide contact surfaces to adsorb more molecules for detection and the metal NPs could be arranged on their surface, which offers a certain number of hot spots. Hence, the 2D nanomaterial system can effectively capture abundant molecules in the sample and adequately amplify the SERS signals, and is identified as an ideal system for SERS detection. The 3D nanomaterials refer to the three dimensions in space of the materials being not at the nanoscale, but consisting of 0D, 1D or 2D nanomaterials [Fig. 10(d)] [108, 109]. Some 3D nanomaterials can be considered as a superposition of multi-layers of monolayer 2D nanomaterials [110, 111], which could get rid of the problems that the 2D SERS-active substrates with a single plane limit their applications. All in all, the key to design SERS-active substrate is to generate more hot spots on the uneven substrates.

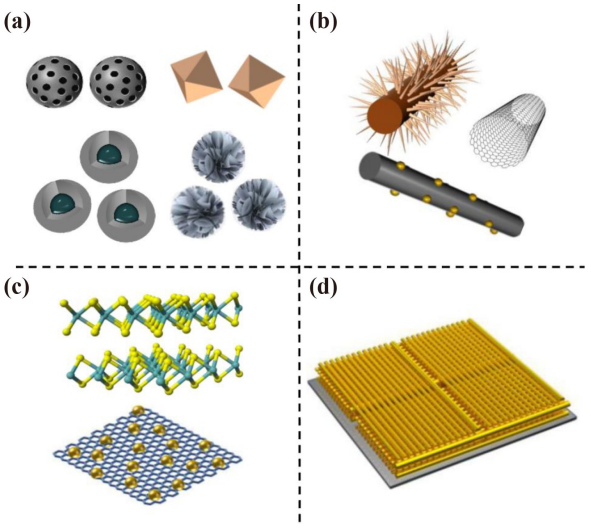

Fig. 10 Schematic diagrams of SERS-active nanomaterials in various dimensions: **(a)** 0 dimension, **(b)** 1 dimension, **(c)** 2 dimensions, **(d)** 3 dimensions. Reproduced with permission from Ref. [109], Copyright © 2020 American Chemical Society.

3.3 Application of SERS in the SARS-CoV-2 detection

The polymerase chain reaction (PCR) is the most commonly used means of detecting SARS-CoV-2 infections, which provides high sensitivity and specificity through the direct quantification of the viral RNA [112], while a pandemic is likely to result in the overloading of PCR testing facilities which can retard pandemic response. Hence, other rapid and relatively accurate virus detection methods are good complement to PCR. Lateral flow immunoassay (LFIAs) [113–118], SERS [112, 119], and terahertz spectroscopy [120–126] are three kinds of typical rapid detection methods. As an alternative to the PCR, LFIAs provide a more rapid response, while their lower sensitivity and specificity for the early infected would lead to delayed diagnosis. Terahertz spectroscopy is a non-invasive, high-sensitivity, and rapid detection method, while it requires careful sample preparation to avoid the interfering signals, and terahertz spectroscopy equipment is not as widely available as other types of spectroscopy equipment, making it less accessible, which leads to limited commercial availability. Compared with the above methods, SERS has advantages of high sensitivity and specificity, non-destructive and

versatility (i.e., detecting a wide range of substances). Owing to its high sensitivity and specificity, SERS sensing technology has been explored in application in the SARS-CoV-2 detection. In 2021, Chen *et al.* [127] developed a SERS-based aptasensor, which enables detecting SARS-CoV-2 with a limit of detection of less than 10 PFU/mL within 15 min. Leong and his colleagues [9] reported a SERS-cased portable breathalyzer [Fig. 11(a)] for mass screening of coronavirus disease (COVID) 2019 under 5 min achieving >95% sensitivity and specificity across 501 participants in 2022. The principle of their experiment is that coronavirus-induced immune responses and metabolic changes can alter concentrations of breath volatile organic compounds (BVOCs) such as 4-mercaptobenzoate (MBA) [Fig. 11(b)], 4-mercaptopyridine (MPY) [Fig. 11(c)], and 4-aminothiophenol (ATP) [Fig. 11(d)], enabling the identification of COVID-positive individuals regardless of their symptoms. Ultrasensitive SERS sensor is key to the experiment. They designed multiple surface receptors on their on-chip SERS sensor, which possess specific functional groups that can chemically interact with BVOCs via hydrogen bonding, ion–dipole interactions and π–π interactions to bring the gaseous analytes close to the plasmonic surface in order to enhance the intensity of SERS. The rapid and high throughput COVID-19 classification is realized via using partial least-squares discriminant analysis. In a word, their work demonstrated a novel way to classify the virus-infected based on SERS of vibrational fingerprints which arise from the interactions between breath metabolites and multiple molecular receptors.

Precisely designed and fabricated plasmonic nanostructures, arranged in a regular pattern with well-defined periodicity and predictable spatial localization of near-field enhancement, are the key for achieving a reproducible and measurable SERS signal. In 2022, Paria and his colleagues [119] reported a label-free spectroscopic SARS-CoV-2 detection on versatile nanoimprinted substrates as shown in Fig. 12. For the design of nanostructures, they discerned the location of the hotspots and determine an estimate of the resonance properties of the nanostructure using finite element methods. To make resonance frequency close to the laser excitation ensuring maximum Raman signal amplification, the plasmonic nanostructures they designed are composed of a field-enhancing metal–insulator antenna

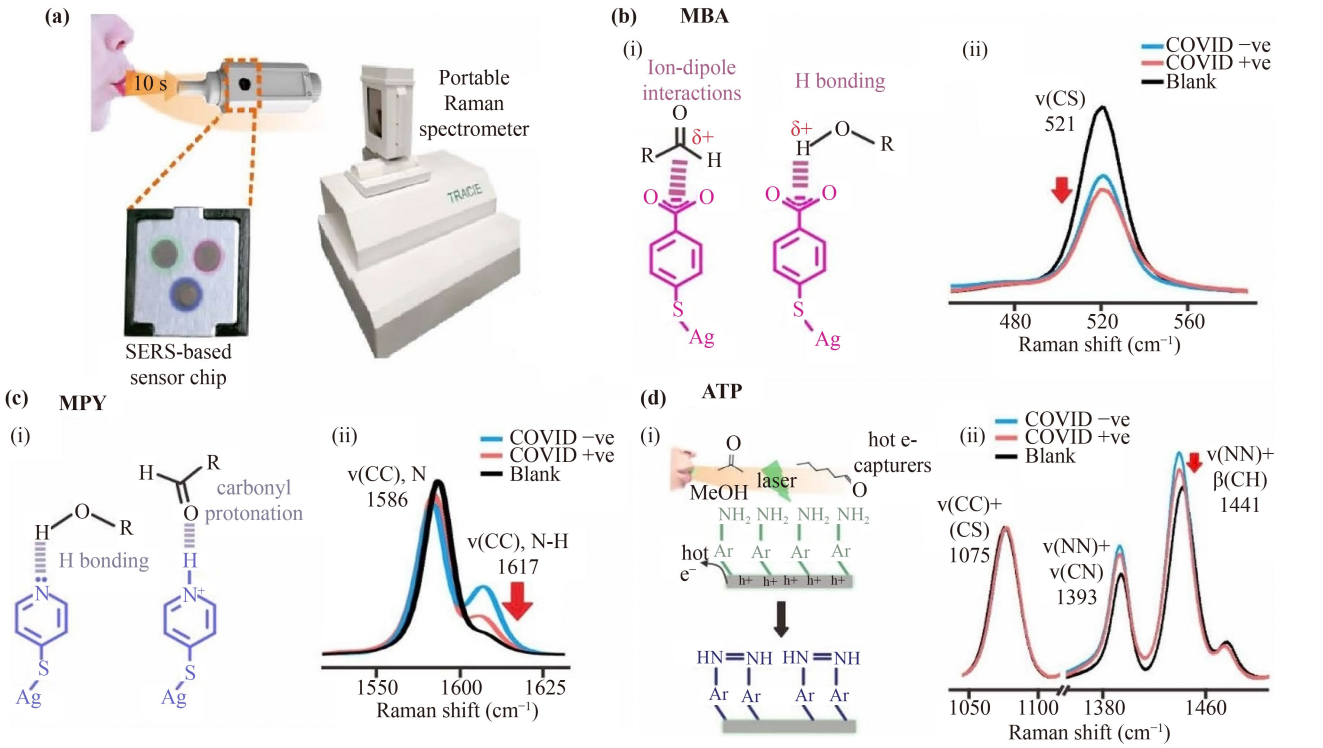

Fig. 11 SERS-based strategy to identify COVID-positive individuals using their breath volatile organic compounds. **(a)** Custom SERS Breathalyzer. **(b)** (i) Ion–dipole interactions between MBA-aldehydes and H-bonding with hydroxyl-containing compounds. (ii) 521 cm^{-1} SERS peak of MBA for blanks, COVID positive and negative breath samples. **(c)** (i) Deprotonated and protonated MPY forming hydrogen bonds with aldehydes and hydroxyl-containing compounds. (ii) MPY I_{1617}/I_{1586} SERS peak intensity ratio for blanks, COVID positive and negative breath samples. **(d)** (i) Increased laser-induced ATP dimerization to DMAB in the presence of breath metabolites that serve as hot electron acceptors. (ii) ATP SERS spectral region at 1030–1600 cm^{-1} for blanks, COVID positive and negative breath samples. Reproduced with permission from Ref. [9], Copyright © 2022 American Chemical Society.

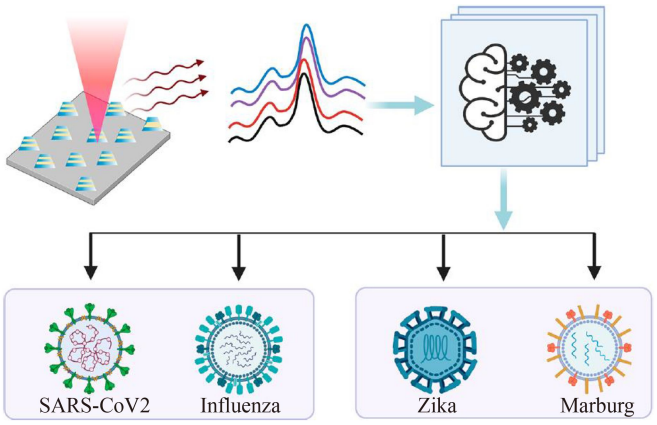

Fig. 12 The detection scheme. SERS signals collected from samples consist of different types of respiratory and nonrespiratory viruses placed on a nano manufactured 2D array of field-enhancing metal–insulator antenna (FEMIA) on a flexible elastomer substrate. Principal component analysis (PCA) and random forest classification were applied on the SERS spectra, which allow us to distinguish and identify different viral samples. Reproduced with permission from Ref. [118], Copyright © 2022 American Chemical Society.

architecture with multiple alternate stacks of silver and silica, which is similar to metal–insulator–metal plasmonic nanoantennas. For the fabrication of the nanostructure, they used nanoimprint lithography and transfer printing. Nanoimprint lithography creates a large area of well-defined nanopatterns in a parallel fashion with a high degree of reproducibility and high throughput, which is an emerging lithography technology invented by Chou and his colleagues [128] in 1996. The large area nano-manufactured flexible sensor surface can be mounted on any surface like doorknobs, cylinders, building entrance, and so forth, to enable on-site rapid testing with a hand-held Raman setup. Moreover, machine learning was used for rapid and accurate detection of SARS-CoV-2. In their study, a random forest algorithm was employed for multiclass classification of the virus spectral data set. For the classification of viral samples, they trained a multiclass random forest classifier with a training set (randomly chosen two-third of the data set) composed of 100 decision trees. The accuracy for the prediction is 99%. Their work provided a method for us to design and fabricate nanostructure in order to gain reproducible and measurable SERS signal. Besides, the machine learning used in their work is an important tool to analyze the Raman signal rapidly, realizing the rapid and accurate detection of SARS-CoV-2.

3.4 Combining SERS with cavity optomechanical sensing

Developing a platform that supports both cavity optomechanical sensing and SERS is attractive, because it could detect and qualitatively analyze nanoparticles with high sensitivity. The cavity optomechanical sensing has drawbacks of low selectivity, while SERS has advantages of high selectivity, which allows for the detection of specific molecules in complex mixture. Cavity optomechanical sensing allows for real-time monitoring of mechanical motion in the cavity. When combined with SERS, this can enable the real-time detection of chemical and biological molecules with high sensitivity and specificity. One possible approach is to use a metallic nanostructure as the mechanical resonator in a cavity optomechanical device. This allows the SERS enhancement to be combined with the sensitivity of cavity optomechanics. Another possible approach is to use SERS-active nanomaterials deposited on a mechanical resonator to enhance the Raman scattering signal of molecules. To our knowledge, there is no relate literatures reporting a platform combining SERS with cavity optomechanical sensing, thus it needs our further research.

As mentioned in Section 2.3, the whispering-gallery microcavity is a kind of important cavity optomechanical platform that could strengthen the light–matter interactions. In 2019, Zhu and his colleagues [128] combine whispering-gallery microcavity, graphene and Ag NPs together as shown in Fig. 13(b), and reached a femtomolar SERS response with an enhancement factor of 0.95×10^{12} and an ultralow detection limit down to 10^{15} M. In this substrate, graphene can improve the SERS signals through charge transfer between the graphene and the

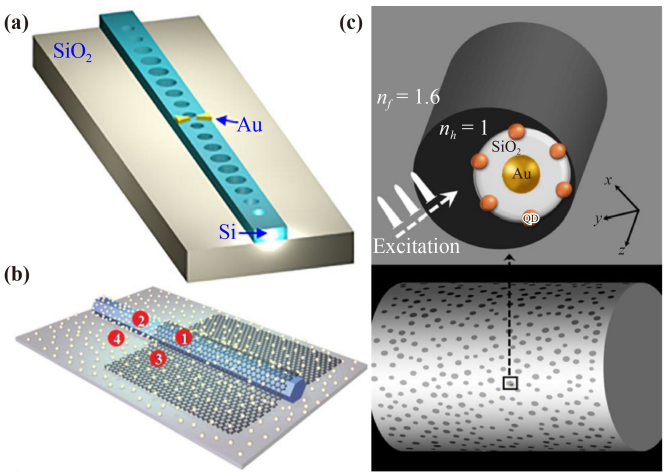

Fig. 13 Potential platforms combining cavity optomechanical sensing with SERS. **(a)** Photonic crystal nanobeam cavity with a plasmonic bowtie antenna. Reproduced with permission from Ref. [129], Copyright © American Institute of Physics 2017. **(b)** ZnO/graphene/Ag-NP hybrid whispering-gallery microcavity. Reproduced with permission from Ref. [128], Copyright © Royal Society of Chemistry 2019. **(c)** Solid Au core/SiO_2 shell nanostructure inside a single hollow nanocavity. Reproduced with permission from Ref. [134], Copyright © Elsevier 2022.

analyte molecules [19, 76, 111] and the whispering-gallery could also enhance the intensity of light, which leads to high sensing performance of the ZnO/graphene/Ag-NP hybrid microcavity. Photonic crystals nanobeam cavities with plasmonic antenna [Figs. 13(a, c)], which could reach exceptionally high quality and low mode volumes [130–133], are also a potential platform to achieve both optomechanical sensing and SERS. In 2021, Cheng *et al.* [134] reported a highly sensitive nanoparticle sensing based on a hybrid plasmonic-photonic cavity in a freely suspended microfiber. Therefore, combining cavity optomechanical sensing with SERS may be feasible in a hybrid microcavity, which could improve the detection frequency range and sensitivity at the same time.

4 Summary and perspective

Detecting the nanoparticles via cavity optomechanical coupling and surface enhanced Raman scattering has been realized in the past several years. The low-frequency vibrational signals of the nanoparticles can be detected by cavity optomechanical platforms, and we can get some information of the nanoparticles, such as the mass, vibrational modes and so on. In this review, we firstly introduced the principle of cavity optomechanical coupling, the principle of cavity optomechanical sensing and the typical optomechanical sensing platforms. Besides, we summarized some state-of-the-art studies on optomechanical sensing the mass, existence and vibrational modes of nanoparticles. Optomechanical sensors, benefiting from their ability of enhancing interactions between light and mechanical oscillators, as well as their small size, scalable production methods, and ability to be integrated with other systems, may have particular potential for the qualitative detection of viruses, such as SARS-CoV-2, which provides a way to improve the sensitivity of detection. The electro-optomechanical coupling platforms combining electrical resonance with external mechanical input will increase tunability and provide more degrees of freedom for sensitivity enhancement, which may be a promising research field of cavity optomechanical sensing. At present, most optomechanical sensing experiments are complemented based on the linear optomechanical coupling effect, thus optomechanical sensing based on quadratic or even higher-order optomechanical coupling effects is also worthy of our in-depth investigation. However, the qualitative detection of nanoparticles by cavity optomechanical coupling has not been realized until now. SERS provides the essential sensitivity to detect a low viral titer, which could not be provided by the spontaneous Raman scattering process. The high-frequency vibrational signals of the nanoparticles can be detected by SERS and we can get the vibrational fingerprint of the nanoparticles. Hence, SERS is an attractive qualitative analytical technique for chemical sensing and biomedical applications. Overall, with the methods of SERS and cavity optomechanical sensing, we can get the information of the nanoparticles from the vibration of the nanoparticles, i.e., detecting nanoparticles by "listening", which has great potential for creating highly sensitive and selective sensors for a range of applications, such as biomedical diagnostics, environmental monitoring, and chemical analysis.

Acknowledgements J. Z. acknowledges the National Key Research and Development Program of China (No. 2017YFA0303401), CAS Interdisciplinary Innovation Team, the National Natural Science Foundation of China (No. 12074371), and the Strategic Priority Research Program of Chinese Academy of Sciences (No. XDB28000000).

References

1. L. He, Ş. K. Özdemir, J. Zhu, W. Kim, and L. Yang, Detecting single viruses and nanoparticles using whispering gallery microlasers, *Nat. Nanotechnol.* 6(7), 428 (2011)
2. L. Shao, X. F. Jiang, X. C. Yu, B. B. Li, W. R. Clements, F. Vollmer, W. Wang, Y. F. Xiao, and Q. Gong, Detection of single nanoparticles and lentiviruses using microcavity resonance broadening, *Adv. Mater.* 25(39), 5616 (2013)
3. W. Chen, Ş. Kaya Özdemir, G. Zhao, J. Wiersig, and L. Yang, Exceptional points enhance sensing in an optical microcavity, *Nature* 548(7666), 192 (2017)
4. M. D. Baaske, P. S. Neu, and M. Orrit, Label-free plasmonic detection of untethered nanometer-sized Brownian particles, *ACS Nano* 14(10), 14212 (2020)
5. W. Yu, W. C. Jiang, Q. Lin, and T. Lu, Cavity optomechanical spring sensing of single molecules, *Nat. Commun.* 7(1), 12311 (2016)
6. C. Cao, J. Zhang, S. Li, and Q. Xiong, Intelligent and ultrasensitive analysis of mercury trace contaminants via plasmonic metamaterial-based surface-enhanced Raman spectroscopy, *Small* 10(16), 3252 (2014)
7. C. Cao, J. Zhang, X. Wen, S. L. Dodson, N. T. Dao, L. M. Wong, S. Wang, S. Li, A. T. Phan, and Q. Xiong, Metamaterials-based label-free nanosensor for conformation and affinity biosensing, *ACS Nano* 7(9), 7583 (2013)
8. S. Sbarra, L. Waquier, S. Suffit, A. Lemaître, and I. Favero, Multimode optomechanical weighting of a single nanoparticle, *Nano Lett.* 22(2), 710 (2022)
9. S. X. Leong, Y. X. Leong, E. X. Tan, H. Y. F. Sim, C. S. L. Koh, Y. H. Lee, C. Chong, L. S. Ng, J. R. T. Chen, D. W. C. Pang, L. B. T. Nguyen, S. K. Boong, X. Han, Y. C. Kao, Y. H. Chua, G. C. Phan-Quang, I. Y. Phang, H. K. Lee, M. Y. Abdad, N. S. Tan, and X. Y. Ling, Noninvasive and point-of-care surface-enhanced raman scattering (SERS)-based breathalyzer for mass screening of coronavirus disease 2019 (COVID-19) under 5 min, *ACS Nano* 16(2), 2629 (2022)
10. E. Gil-Santos, J. J. Ruz, O. Malvar, I. Favero, A. Lemaître, P. M. Kosaka, S. García-López, M. Calleja, and J. Tamayo, Optomechanical detection of vibration modes of a single bacterium, *Nat. Nanotechnol.* 15(6), 469 (2020)

11. L. Wang, X. Wang, Y. Wu, M. Guo, C. Gu, C. Dai, D. Kong, Y. Wang, C. Zhang, D. Qu, C. Fan, Y. Xie, Z. Zhu, Y. Liu, and D. Wei, Rapid and ultrasensitive electromechanical detection of ions, biomolecules and SARS-CoV-2 RNA in unamplified samples, *Nat. Biomed. Eng.* 6(3), 276 (2022)
12. J. Zhang, C. Cao, X. Xu, C. Liow, S. Li, P. Tan, and Q. Xiong, Tailoring alphabetical metamaterials in optical frequency: Plasmonic coupling, dispersion, and sensing, *ACS Nano* 8(4), 3796 (2014)
13. P. Wang, S. Chen, M. Guo, S. Peng, M. Wang, M. Chen, W. Ma, R. Zhang, J. Su, X. Rong, F. Shi, T. Xu, and J. Du, Nanoscale magnetic imaging of ferritins in a single cell, *Sci. Adv.* 5(4), eaau8038 (2019)
14. D. Le Sage, K. Arai, D. R. Glenn, S. J. DeVience, L. M. Pham, L. Rahn-Lee, M. D. Lukin, A. Yacoby, A. Komeili, and R. L. Walsworth, Optical magnetic imaging of living cells, *Nature* 496, 486 (2013)
15. X. Jiang, A. J. Qavi, S. H. Huang, and L. Yang, Whispering-gallery sensors, *Matter* 3(2), 371 (2020)
16. K. Ekinci, Electromechanical transducers at the nanoscale: Actuation and sensing of motion in nanoelectromechanical systems (NEMS), *Small* 1(8-9), 786 (2005)
17. M. P. Blencowe, Nanoelectromechanical systems, *Contemp. Phys.* 46(4), 249 (2005)
18. C. Anichini, W. Czepa, D. Pakulski, A. Aliprandi, A. Ciesielski, and P. Samorì, Chemical sensing with 2D materials, *Chem. Soc. Rev.* 47(13), 4860 (2018)
19. Y. Ohno, K. Maehashi, and K. Matsumoto, Label-free biosensors based on aptamer-modified graphene field-effect transistors, *J. Am. Chem. Soc.* 132(51), 18012 (2010)
20. J. M. Lai, Y. J. Sun, Q. H. Tan, P. H. Tan, and J. Zhang, Laser cooling of a lattice vibration in van der Waals semiconductor, *Nano Lett.* 22(17), 7129 (2022)
21. J. M. Lai, M. U. Farooq, Y. J. Sun, P. H. Tan, and J. Zhang, Multiphonon process in Mn-doped ZnO nanowires, *Nano Lett.* 22(13), 5385 (2022)
22. J. Zhang, Q. Zhang, X. Wang, L. C. Kwek, and Q. Xiong, Resolved-sideband Raman cooling of an optical phonon in semiconductor materials, *Nat. Photonics* 10(9), 600 (2016)
23. J. J. Li and K. D. Zhu, Nonlinear optical mass sensor with an optomechanical microresonator, *Appl. Phys. Lett.* 101(14), 141905 (2012)
24. S. Liu, B. Liu, J. Wang, T. Sun, and W. X. Yang, Realization of a highly sensitive mass sensor in a quadratically coupled optomechanical system, *Phys. Rev. A* 99(3), 033822 (2019)
25. B. B. Li, L. Ou, Y. Lei, and Y. C. Liu, Cavity optomechanical sensing, *Nanophotonics* 10(11), 2799 (2021)
26. Y. W. Hu, Y. F. Xiao, Y. C. Liu, and Q. Gong, Optomechanical sensing with on-chip microcavities, *Front. Phys.* 8(5), 475 (2013)
27. F. Liu, S. Alaie, Z. C. Leseman, and M. Hossein-Zadeh, Sub-pg mass sensing and measurement with an optomechanical oscillator, *Opt. Express* 21(17), 19555 (2013)
28. P. Djorwe, Y. Pennec, and B. Djafari-Rouhani, Exceptional point enhances sensitivity of optomechanical mass sensors, *Phys. Rev. Appl.* 12(2), 024002 (2019)
29. M. Sansa, M. Defoort, A. Brenac, M. Hermouet, L. Banniard, A. Fafin, M. Gely, C. Masselon, I. Favero, G. Jourdan, and S. Hentz, Optomechanical mass spectrometry, *Nat. Commun.* 11(1), 3781 (2020)
30. F. Liu and M. Hossein-Zadeh, Mass sensing with optomechanical oscillation, *IEEE Sens. J.* 13(1), 146 (2013)
31. L. Lan, Y. Gao, X. Fan, M. Li, Q. Hao, and T. Qiu, The origin of ultrasensitive SERS sensing beyond plasmonics, *Front. Phys.* 16(4), 43300 (2021)
32. M. Aspelmeyer, T. J. Kippenberg, and F. Marquardt, Cavity optomechanics, *Rev. Mod. Phys.* 86(4), 1391 (2014)
33. H. Chang and J. Zhang, From cavity optomechanics to cavity-less exciton optomechanics: A review, *Nanoscale* 14(45), 16710 (2022)
34. Y. F. Gao, J. M. Lai, and J. Zhang, Optical control of bulk phonon modes in crystalline solids, *Adv. Quantum Technol.* 5(2), 2100103 (2022)
35. D. Yu, M. Humar, K. Meserve, R. C. Bailey, S. N. Chormaic, and F. Vollmer, Whispering-gallery-mode sensors for biological and physical sensing, *Nat. Rev. Methods Primers* 1(1), 83 (2021)
36. H. Miao, K. Srinivasan, and V. Aksyuk, A microelectromechanically controlled cavity optomechanical sensing system, *New J. Phys.* 14(7), 075015 (2012)
37. X. Han, W. Fu, C. Zhong, C. L. Zou, Y. Xu, A. A. Sayem, M. Xu, S. Wang, R. Cheng, L. Jiang, and H. X. Tang, Cavity piezo-mechanics for superconducting-nanophotonic quantum interface, *Nat. Commun.* 11(1), 3237 (2020)
38. C. Bekker, R. Kalra, C. Baker, and W. P. Bowen, Injection locking of an electro-optomechanical device, *Optica* 4(10), 1196 (2017)
39. J. Chae, S. An, G. Ramer, V. Stavila, G. Holland, Y. Yoon, A. A. Talin, M. Allendorf, V. A. Aksyuk, and A. Centrone, Nanophotonic atomic force microscope transducers enable chemical composition and thermal conductivity measurements at the nanoscale, *Nano Lett.* 17(9), 5587 (2017)
40. A. G. Krause, M. Winger, T. D. Blasius, Q. Lin, and O. Painter, A high-resolution microchip optomechanical accelerometer, *Nat. Photonics* 6(11), 768 (2012)
41. X. Liu, W. Liu, Z. Ren, Y. Ma, B. Dong, G. Zhou, and C. Lee, Progress of optomechanical micro/nano sensors: A review, *Int. J. Optomechatronics* 15(1), 120 (2021)
42. W. Xiang and C. Lee, Nanophotonics sensor based on microcantilever for chemical analysis, *IEEE J. Sel. Top. Quantum Electron.* 15(5), 1323 (2009)
43. T. T. Mai, F. L. Hsiao, C. Lee, W. Xiang, C. C. Chen, and W. Choi, Optimization and comparison of photonic crystal resonators for silicon microcantilever sensors, *Sens. Actuators A Phys.* 165(1), 16 (2011)
44. D. Yang, X. Liu, X. Li, B. Duan, A. Wang, and Y. Xiao, Photoic crystal nanobeam cavity devices for on-chip integrated silicon photonics, *J. Semicond.* 42(2), 023103 (2021)
45. F. J. Giessibl, Advances in atomic force microscopy, *Rev. Mod. Phys.* 75(3), 949 (2003)
46. Z. Zhao, H. Chang, R. Wang, P. Du, X. He, J. Yang,

X. Zhang, K. Huang, D. Fan, Y. Wang, X. Pan, and M. Lei, Activity origin and catalyst design principles for electrocatalytic oxygen evolution on layered transition metal oxide with halogen doping, *Small Struct.* 2(9), 2100069 (2021)
47. Y. Chen, Z. Shen, X. Xiong, C. H. Dong, C. L. Zou, and G. C. Guo, Mechanical bound state in the continuum for optomechanical microresonators, *New J. Phys.* 18(6), 063031 (2016)
48. M. Zhao and K. Fang, Mechanical bound states in the continuum for macroscopic optomechanics, *Opt. Express* 27(7), 10138 (2019)
49. Y. Yu, X. Xi, and X. Sun, Observation of mechanical bound states in the continuum in an optomechanical microresonator, *Light Sci. Appl.* 11(1), 328 (2022)
50. S. Liu, H. Tong, and K. Fang, Optomechanical crystal with bound states in the continuum, *Nat. Commun.* 13(1), 3187 (2022)
51. S. Zanotto, G. Conte, L. Bellieres, A. Griol, D. Navarro-Urrios, A. Tredicucci, A. Martínez, and A. Pitanti, Optomechanical modulation spectroscopy of bound states in the continuum in a dielectric metasurface, *Phys. Rev. Appl.* 17(4), 044033 (2022)
52. H. Chang, Z. Li, W. Lou, Q. Yao, J. M. Lai, B. Liu, H. Ni, Z. Niu, K. Chang, and J. Zhang, Terahertz cavity optomechanics using a topological nanophononic superlattice, *Nanoscale* 14(36), 13046 (2022)
53. M. Esmann, F. Lamberti, A. Harouri, L. Lanco, I. Sagnes, I. Favero, G. Aubin, C. Gomez-Carbonell, A. Lemaitre, O. Krebs, P. Senellart, and N. D. Lanzillotti-Kimura, Brillouin scattering in hybrid optophononic Bragg micropillar resonators at 300 GHz, *Optica* 6(7), 854 (2019)
54. A. Rodriguez, P. Priya, O. Ortiz, P. Senellart, C. Gomez-Carbonell, A. Lemaitre, M. Esmann, and N. Lanzillotti-Kimura, Fiber-based angular filtering for high-resolution Brillouin spectroscopy in the 20–300 GHz frequency range, *Opt. Express* 29(2), 2637 (2021)
55. Y. M. Bar-On, A. Flamholz, R. Phillips, and R. Milo, SARS-CoV-2 (COVID-19) by the numbers, *elife* 9, e57309 (2020)
56. J. C. Sankey, C. Yang, B. M. Zwickl, A. M. Jayich, and J. G. Harris, Strong and tunable nonlinear optomechanical coupling in a low-loss system, *Nat. Phys.* 6(9), 707 (2010)
57. G. Brawley, M. Vanner, P. E. Larsen, S. Schmid, A. Boisen, and W. Bowen, Nonlinear optomechanical measurement of mechanical motion, *Nat. Commun.* 7(1), 10988 (2016)
58. R. Burgwal, J. del Pino, and E. Verhagen, Comparing nonlinear optomechanical coupling in membrane-in-the-middle and single-cavity systems, *New J. Phys.* 22(11), 113006 (2020)
59. K. Børkje, A. Nunnenkamp, J. Teufel, and S. Girvin, Signatures of nonlinear cavity optomechanics in the weak coupling regime, *Phys. Rev. Lett.* 111(5), 053603 (2013)
60. C. Doolin, B. Hauer, P. Kim, A. MacDonald, H. Ramp, and J. Davis, Nonlinear optomechanics in the stationary regime, *Phys. Rev. A* 89(5), 053838 (2014)
61. S. Shahidani, M. Naderi, and M. Soltanolkotabi, Control and manipulation of electromagnetically induced transparency in a nonlinear optomechanical system with two movable mirrors, *Phys. Rev. A* 88(5), 053813 (2013)
62. S. Shahidani, M. Naderi, M. Soltanolkotabi, and S. Barzanjeh, Steady-state entanglement, cooling, and tristability in a nonlinear optomechanical cavity, *J. Opt. Soc. Am. B* 31(5), 1087 (2014)
63. M. R. Vanner, Selective linear or quadratic optomechanical coupling via measurement, *Phys. Rev. X* 1(2), 021011 (2011)
64. M. Tan, X. Xu, J. Wu, T. G. Nguyen, S. T. Chu, B. E. Little, R. Morandotti, A. Mitchell, and D. J. Moss, Photonic radio frequency channelizers based on Kerr optical micro-combs, *J. Semicond.* 42(4), 041302 (2021)
65. J. F. Rhoads and S. W. Shaw, The impact of nonlinearity on degenerate parametric amplifiers, *Appl. Phys. Lett.* 96(23), 234101 (2010)
66. K. Wódkiewicz and M. S. Zubairy, Effect of laser fluctuations on squeezed states in a degenerate parametric amplifier, *Phys. Rev. A* 27(4), 2003 (1983)
67. M. Bhattacharya, H. Uys, and P. Meystre, Optomechanical trapping and cooling of partially reflective mirrors, *Phys. Rev. A* 77(3), 033819 (2008)
68. S. Huang and G. Agarwal, Electromagnetically induced transparency from two-phonon processes in quadratically coupled membranes, *Phys. Rev. A* 83(2), 023823 (2011)
69. J. Thompson, B. Zwickl, A. Jayich, F. Marquardt, S. Girvin, and J. Harris, Strong dispersive coupling of a high-finesse cavity to a micromechanical membrane, *Nature* 452(7183), 72 (2008)
70. D. Xu and Y. F. Xiao, Listening to the sound of a bacterium, *Nat. Nanotechnol.* 15(6), 420 (2020)
71. Y. Li, L. Zhao, Y. Yao, and X. Guo, Single-molecule nanotechnologies: An evolution in biological dynamics detection, *ACS Appl. Bio Mater.* 3(1), 68 (2020)
72. L. A. Lyon, C. D. Keating, A. P. Fox, B. E. Baker, L. He, S. R. Nicewarner, S. P. Mulvaney, and M. J. Natan, Raman spectroscopy, *Anal. Chem.* 70(12), 341 (1998)
73. X. Zhang, X. F. Qiao, W. Shi, J. B. Wu, D. S. Jiang, and P. H. Tan, Phonon and Raman scattering of two-dimensional transition metal dichalcogenides from monolayer, multilayer to bulk material, *Chem. Soc. Rev.* 44(9), 2757 (2015)
74. R. S. Das and Y. Agrawal, Raman spectroscopy: Recent advancements, techniques and applications, *Vib. Spectrosc.* 57(2), 163 (2011)
75. Z. Movasaghi, S. Rehman, and I. U. Rehman, Raman spectroscopy of biological tissues, *Appl. Spectrosc. Rev.* 42(5), 493 (2007)
76. L. M. Malard, M. A. Pimenta, G. Dresselhaus, and M. S. Dresselhaus, Raman spectroscopy in graphene, *Phys. Rep.* 473(5-6), 51 (2009)
77. X. X. Han, R. S. Rodriguez, C. L. Haynes, Y. Ozaki, and B. Zhao, Surface-enhanced Raman spectroscopy, *Nat. Rev. Methods Primers* 1(1), 87 (2022)
78. E. S. Allakhverdiev, V. V. Khabatova, B. D. Kossalbayev, E. V. Zadneprovskaya, O. V. Rodnenkov, T. V.

Martynyuk, G. V. Maksimov, S. Alwasel, T. Tomo, and S. I. Allakhverdiev, Raman spectroscopy and its modifications applied to biological and medical research, *Cells* 11(3), 386 (2022)
79. J. Plou, P. S. Valera, I. García, C. D. de Albuquerque, A. Carracedo, and L. M. Liz-Marzán, Prospects of surface-enhanced Raman spectroscopy for biomarker monitoring toward precision medicine, *ACS Photonics* 9(2), 333 (2022)
80. R. Maher, C. Galloway, E. Le Ru, L. Cohen, and P. Etchegoin, Vibrational pumping in surface enhanced Raman scattering (SERS), *Chem. Soc. Rev.* 37(5), 965 (2008)
81. R. F. Aroca, Plasmon enhanced spectroscopy, *Phys. Chem. Chem. Phys.* 15(15), 5355 (2013)
82. M. Li, S. K. Cushing, and N. Wu, Plasmon-enhanced optical sensors: a review, *Analyst (Lond.)* 140(2), 386 (2015)
83. F. Benz, M. K. Schmidt, A. Dreismann, R. Chikkaraddy, Y. Zhang, A. Demetriadou, C. Carnegie, H. Ohadi, B. De Nijs, R. Esteban, J. Aizpurua, and J. J. Baumberg, Single-molecule optomechanics in "picocavities", *Science* 354(6313), 726 (2016)
84. Y. S. Yamamoto, Y. Ozaki, and T. Itoh, Recent progress and frontiers in the electromagnetic mechanism of surface-enhanced Raman scattering, *J. Photochem. Photobiol. Photochem. Rev.* 21, 81 (2014)
85. B. Sharma, R. R. Frontiera, A. I. Henry, E. Ringe, and R. P. Van Duyne, SERS: Materials, applications, and the future, *Mater. Today* 15(1–2), 16 (2012)
86. X. Yu, H. Cai, W. Zhang, X. Li, N. Pan, Y. Luo, X. Wang, and J. Hou, Tuning chemical enhancement of SERS by controlling the chemical reduction of graphene oxide nanosheets, *ACS Nano* 5(2), 952 (2011)
87. L. Xia, M. Chen, X. Zhao, Z. Zhang, J. Xia, H. Xu, and M. Sun, Visualized method of chemical enhancement mechanism on SERS and TERS, *J. Spectrosc.* 45, 533 (2014)
88. B. Dong, L. Liu, H. Xu, and M. Sun, Experimental and theoretical evidence for the chemical mechanism in SERRS of rhodamine 6G adsorbed on colloidal silver excited at 1064 nm, *J. Spectrosc.* 41, 719 (2010)
89. P. Roelli, C. Galland, N. Piro, and T. J. Kippenberg, Molecular cavity optomechanics as a theory of plasmon-enhanced Raman scattering, *Nat. Nanotechnol.* 11(2), 164 (2016)
90. R. Esteban, J. J. Baumberg, and J. Aizpurua, Molecular optomechanics approach to surface-enhanced Raman scattering, *Acc. Chem. Res.* 55(14), 1889 (2022)
91. Z. Huang, A. Zhang, Q. Zhang, and D. Cui, Nanomaterial-based SERS sensing technology for biomedical application, *J. Mater. Chem. B* 7(24), 3755 (2019)
92. S. W. Joo, W. J. Kim, W. S. Yoon, and I. S. Choi, Adsorption of 4, 4′-biphenyl diisocyanide on gold nanoparticle surfaces investigated by surface-enhanced Raman scattering, *J. Raman Spectrosc.* 34(4), 271 (2003)
93. S. K. Venkata, S. A. Gaddam, V. S. Kotakadi, and D. Gopal, Multifunctional silver nanoparticles by fruit extract of terminalia belarica and their therapeutic applications: A 3-in-1 system, *Nano Biomed. Eng.* 10(3), 279 (2018)
94. S. Nie and S. R. Emory, Probing single molecules and single nanoparticles by surface-enhanced Raman scattering, *Science* 275(5303), 1102 (1997)
95. C. Song, N. Zhou, B. Yang, Y. Yang, and L. Wang, Facile synthesis of hydrangea flower-like hierarchical gold nanostructures with tunable surface topographies for single-particle surface-enhanced Raman scattering, *Nanoscale* 7(40), 17004 (2015)
96. H. Liang, Z. Li, W. Wang, Y. Wu, and H. Xu, Highly surface-roughened "flower-like" silver nanoparticles for extremely sensitive substrates of surface-enhanced Raman scattering, *Adv. Mater.* 21(45), 4614 (2009)
97. C. Hu, J. Shen, J. Yan, J. Zhong, W. Qin, R. Liu, A. Aldalbahi, X. Zuo, S. Song, C. Fan, and D. He, Highly narrow nanogap-containing Au@ Au core–shell SERS nanoparticles: Size-dependent Raman enhancement and applications in cancer cell imaging, *Nanoscale* 8(4), 2090 (2016)
98. J. Chang, A. Zhang, Z. Huang, Y. Chen, Q. Zhang, and D. Cui, Monodisperse Au@Ag core-shell nanoprobes with ultrasensitive SERS-activity for rapid identification and Raman imaging of living cancer cells, *Talanta* 198, 45 (2019)
99. B. Chen, G. Meng, Q. Huang, Z. Huang, Q. Xu, C. Zhu, Y. Qian, and Y. Ding, Green synthesis of large-scale highly ordered core@shell nanoporous Au@Ag nanorod arrays as sensitive and reproducible 3D SERS substrates, *ACS Appl. Mater. Interfaces* 6(18), 15667 (2014)
100. Y. Yang, Q. Zhang, Z. W. Fu, and D. Qin, Transformation of Ag nanocubes into Ag–Au hollow nanostructures with enriched Ag contents to improve SERS activity and chemical stability, *ACS Appl. Mater. Interfaces* 6(5), 3750 (2014)
101. J. M. Li, Y. Yang, and D. Qin, Hollow nanocubes made of Ag–Au alloys for SERS detection with sensitivity of 10– 8 M for melamine, *J. Mater. Chem. C* 2(46), 9934 (2014)
102. X. X. Han, W. Ji, B. Zhao, and Y. Ozaki, Semiconductor-enhanced Raman scattering: Active nanomaterials and applications, *Nanoscale* 9(15), 4847 (2017)
103. T. Kang, S. M. Yoo, I. Yoon, S. Y. Lee, and B. Kim, Patterned multiplex pathogen DNA detection by Au particle-on-wire SERS sensor, *Nano Lett.* 10(4), 1189 (2010)
104. Z. Jiang, Q. Zhang, C. Zong, B. J. Liu, B. Ren, Z. Xie, and L. Zheng, Cu–Au alloy nanotubes with five-fold twinned structure and their application in surface-enhanced Raman scattering, *J. Mater. Chem.* 22(35), 18192 (2012)
105. P. K. Kannan, P. Shankar, C. Blackman, and C. H. Chung, Recent advances in 2D inorganic nanomaterials for SERS sensing, *Adv. Mater.* 31(34), 1803432 (2019)
106. X. Cai, X. Han, C. Zhao, C. Niu, and Y. Jia, Tellurene: An elemental 2D monolayer material beyond its bulk phases without van der Waals layered structures, *J. Semicond.* 41(8), 081002 (2020)
107. Z. Li, J. M. Lai, and J. Zhang, Review of phonons in moiré superlattices, *J. Semicond.* 44(1), 011902 (2023)
108. Z. Li, S. Jiang, Y. Huo, T. Ning, A. Liu, C. Zhang, Y.

He, M. Wang, C. Li, and B. Man, 3D silver nanoparticles with multilayer graphene oxide as a spacer for surface enhanced Raman spectroscopy analysis, *Nanoscale* 10(13), 5897 (2018)

109. X. Liang, Y. S. Wang, T. T. You, X. J. Zhang, N. Yang, G. S. Wang, and P. G. Yin, Interfacial synthesis of a three-dimensional hierarchical MoS_2-NS@Ag-NP nanocomposite as a SERS nanosensor for ultrasensitive thiram detection, *Nanoscale* 9(25), 8879 (2017)
110. H. J. Park, S. Cho, M. Kim, and Y. S. Jung, Carboxylic acid-functionalized, graphitic layer-coated three-dimensional SERS substrate for label-free analysis of Alzheimer's disease biomarkers, *Nano Lett.* 20(4), 2576 (2020)
111. E. Zhang, Z. Xing, D. Wan, H. Gao, Y. Han, Y. Gao, H. Hu, Z. Cheng, and T. Liu, Surface-enhanced Raman spectroscopy chips based on two-dimensional materials beyond graphene, *J. Semicond.* 42(5), 051001 (2021)
112. A. Idili, C. Parolo, R. Alvarez-Diduk, and A. Merkoçi, Rapid and efficient detection of the SARS-CoV-2 spike protein using an electrochemical aptamer-based sensor, *ACS Sens.* 6(8), 3093 (2021)
113. T. T. Tsai, T. H. Huang, C. A. Chen, N. Y. J. Ho, Y. J. Chou, and C. F. Chen, Development a stacking pad design for enhancing the sensitivity of lateral flow immunoassay, *Sci. Rep.* 8(1), 17319 (2018)
114. I. Montesinos, D. Gruson, B. Kabamba, H. Dahma, S. Van den Wijngaert, S. Reza, V. Carbone, O. Vandenberg, B. Gulbis, F. Wolff, and H. Rodriguez-Villalobos, Evaluation of two automated and three rapid lateral flow immunoassays for the detection of anti-SARS-CoV-2 antibodies, *J. Clin. Virol.* 128, 104413 (2020)
115. L. Anfossi, C. Baggiani, C. Giovannoli, G. D'Arco, and G. Giraudi, Lateral-flow immunoassays for mycotoxins and phycotoxins: A review, *Anal. Bioanal. Chem.* 405(2-3), 467 (2013)
116. D. Wang, S. He, X. Wang, Y. Yan, J. Liu, S. Wu, S. Liu, Y. Lei, M. Chen, L. Li, J. Zhang, L. Zhang, X. Hu, X. Zheng, J. Bai, Y. Zhang, Y. Zhang, M. Song, and Y. Tang, Rapid lateral flow immunoassay for the fluorescence detection of SARS-CoV-2 RNA, *Nat. Biomed. Eng.* 4(12), 1150 (2020)
117. R. Banerjee and A. Jaiswal, Recent advances in nanoparticle-based lateral flow immunoassay as a point-of-care diagnostic tool for infectious agents and diseases, *Analyst (Lond.)* 143(9), 1970 (2018)
118. F. Di Nardo, M. Chiarello, S. Cavalera, C. Baggiani, and L. Anfossi, Ten years of lateral flow immunoassay technique applications: Trends, challenges and future perspectives, *Sensors (Basel)* 21(15), 5185 (2021)
119. D. Paria, K. S. Kwok, P. Raj, P. Zheng, D. H. Gracias, and I. Barman, Label-free spectroscopic SARS-CoV-2 detection on versatile nanoimprinted substrates, *Nano Lett.* 22(9), 3620 (2022)
120. M. Walther, B. M. Fischer, A. Ortner, A. Bitzer, A. Thoman, and H. Helm, Chemical sensing and imaging with pulsed terahertz radiation, *Anal. Bioanal. Chem.* 397(3), 1009 (2010)
121. D. J. Tyree, P. Huntington, J. Holt, A. L. Ross, R. Schueler, D. T. Petkie, S. S. Kim, C. C. Grigsby, C. Neese, and I. R. Medvedev, Terahertz spectroscopic molecular sensor for rapid and highly specific quantitative analytical gas sensing, *ACS Sens.* 7(12), 3730 (2022)
122. M. Beruete and I. Jáuregui-López, Terahertz sensing based on metasurfaces, *Adv. Opt. Mater.* 8(3), 1900721 (2020)
123. H. B. Liu, H. Zhong, N. Karpowicz, Y. Chen, and X. C. Zhang, Terahertz spectroscopy and imaging for defense and security applications, *Proc. IEEE* 95(8), 1514 (2007)
124. V. Vaks, V. Anfertev, M. Chernyaeva, E. Domracheva, A. Yablokov, A. Maslennikova, A. Zhelesnyak, A. Baranov, Y. Schevchenko, and M. F. Pereira, Sensing nitriles with THz spectroscopy of urine vapours from cancers patients subject to chemotherapy, *Sci. Rep.* 12(1), 18117 (2022)
125. A. Toma, S. Tuccio, M. Prato, F. De Donato, A. Perucchi, P. Di Pietro, S. Marras, C. Liberale, R. Proietti Zaccaria, F. De Angelis, L. Manna, S. Lupi, E. Di Fabrizio, and L. Razzari, Squeezing terahertz light into nanovolumes: Nanoantenna enhanced terahertz spectroscopy (NETS) of semiconductor quantum dots, *Nano Lett.* 15(1), 386 (2015)
126. J. Liu, J. Dai, S. L. Chin, and X. C. Zhang, Broadband terahertz wave remote sensing using coherent manipulation of fluorescence from asymmetrically ionized gases, *Nat. Photonics* 4(9), 627 (2010)
127. H. Chen, S. G. Park, N. Choi, H. J. Kwon, T. Kang, M. K. Lee, and J. Choo, Sensitive detection of SARS-CoV-2 using a SERS-based aptasensor, *ACS Sens.* 6(6), 2378 (2021)
128. S. Y. Chou, P. R. Krauss, and P. J. Renstrom, Nanoimprint lithography, *J. Vac. Sci. Technol. B* 14(6), 4129 (1996)
129. Q. Zhu, C. Xu, D. Wang, B. Liu, F. Qin, Z. Zhu, Y. Liu, X. Zhao, and Z. Shi, Femtomolar response of a plasmon-coupled ZnO/graphene/silver hybrid whispering-gallery mode microcavity for SERS sensing, *J. Mater. Chem. C* 7(9), 2710 (2019)
130. D. Conteduca, C. Reardon, M. G. Scullion, F. Dell' Olio, M. N. Armenise, T. F. Krauss, and C. Ciminelli, Ultra-high Q/V hybrid cavity for strong light-matter interaction, *APL Photonics* 2(8), 086101 (2017)
131. X. Xiong and Y. F. Xiao, Hybrid plasmonic-photonic microcavity for enhanced light-matter interaction, *Sci. Bull. (Beijing)* 67(12), 1205 (2022)
132. H. Zhang, W. Zhao, Y. Liu, J. Chen, X. Wang, and C. Lu, Photonic-plasmonic hybrid microcavities: Physics and applications, *Chin. Phys. B* 30(11), 117801 (2021)
133. Z. Li, H. Chang, J. M. Lai, F. Song, Q. Yao, H. Liu, H. Ni, Z. Niu, and J. Zhang, Terahertz phononic crystal in plasmonic nanocavity, *J. Semicond.* (2023) (in press)
134. Q. Cheng, S. Wang, J. Lv, J. Wang, and N. Liu, Highly sensitive nanoparticle sensing based on a hybrid cavity in a freely suspended microfiber, *Nanotechnology* 32(20), 205203 (2021)
135. B. Gökbulut, A. Inanç, G. Topcu, S. Ozcelik, M. M. Demir, and M. N. Inci, Hybrid photonic-plasmonic mode-coupling induced enhancement of the spontaneous emission rate of CdS/CdSe quantum emitters, *Physica E* 136, 115017 (2022)